2015

Conservation Laws and Electromagnetic Interactions

Veerachart Kajorndejnukul
University of Central Florida

CONSERVATION LAWS AND ELECTROMAGNETIC INTERACTIONS

by

VEERACHART KAJORNDEJNUKUL
B. S. Chulalongkorn University, 2009
M.S. University of Central Florida, 2011

A dissertation submitted in partial fulfillment of the requirements
for the degree of Doctor of Philosophy
in CREOL, the College of Optics & Photonics
at the University of Central Florida
Orlando, Florida

Fall Term
2015

Major Professor: Aristide Dogariu

ABSTRACT

Aside from energy, light carries linear and angular momenta that can be transferred to matter. The interaction between light and matter is governed by conservation laws that can manifest themselves as mechanical effects acting on both matter and light waves. This interaction permits remote, precise, and noninvasive manipulation and sensing at microscopic levels. In this dissertation, we demonstrated for the first time a complete set of opto-mechanical effects that are based on nonconservative forces and act at the interface between dielectric media. Without structuring the light field, forward action is provided by the conventional radiation pressure while a backward movement can be achieved through the natural enhancement of linear momentum. If the symmetry of scattered field is broken, a side motion can also be induced due to the transformation between spin and orbital angular momenta. In experiments, these opto-mechanical effects can be significantly amplified by the long-range hydrodynamic interactions that provide an efficient recycling of energy. These unusual opto-mechanical effects open new possibilities for efficient manipulation of colloidal microparticles without having to rely on intricate structuring or shaping of light beams. Optically-controlled transport of matter is sought after in diverse applications in biology, colloidal physics, chemistry, condensed matter and others.

Another consequence of light-matter interaction is the modification of the optical field itself, which can manifest, for instance, as detectable shifts of the centroids of optical beams during reflection and refraction. The spin-Hall effect of light (SHEL) is one type of such beam shifts that is due to the spin-orbit transformation governed by the conservation of angular momentum. We have shown that this effect can be amplified by the structural anisotropy of random nanocomposite materials.

ACKNOWLEDGEMENT

One of many things that I have learnt throughout my Ph.D. study at CREOL, UCF, is that surrounding with talented and good people makes you produce high-quality research works easier. It is fortunate that this applies to me. I would like to take this opportunity to thank many people.

First, I would like to thank Dr. Aristide Dogariu, who is my Ph.D. advisor, for his guidance and support. He has been teaching me many things including how to think logically, systematically, and scientifically, and how to organize everything. I strongly believe this will strengthen my academic career.

I would like to thank our random group from the past and present for their genuine support. They are like my second family here.

I would like to thank my Thai friends here, Tua, Bo, and P' First.

I would like to thank my love, Nok, for always being beside me no matter what I have gone through.

Lastly, I would like to thank my parents for providing me the highest education and teaching me to be a good person.

TABLE OF CONTENTS

LIST OF FIGURES

LIST OF ABBREVIATIONS

OT	Optical Tweezer
SLMs	Spatial Light Modulators
HOT	Holographic Optical Tweezer
SAM	Spin Angular Momentum
OAM	Orbital Angular Momentum
AM	Angular Momentum
AB	Aharonov-Bohm
CMOS	Complementary metal-oxide semiconductor
SOI	Spin-Orbit Interaction
CCD	Charge-Coupled Device
DDA	Discrete Dipole Approximation
NA	Numerical aperture
CW	Continuous wave
OD	Optical density
GH	Goos-Hanchen
IF	Imbert-Fedorov
SHEL	Spin Hall Effect of Light
SIA	Surface Induced Anisotropy
FEM	Finite Elements Methods
MGT	Maxwell Garnett theory
MGEM	Maxwell Garnett Effective Medium Theory

CHAPTER 1: LIGHT-MATTER INTERACTIONS IN DIELECTRICS: MECHANICAL ACTION OF LIGHT

The mechanical effect of light has been early realized since an observation by Johannes Kepler in 1619. He suggested that solar radiations push away tail of a comet from the sun. After that, a series of key studies by Einstein, Compton, and Frisch established that light can be quantized as photon possessing energy and momentum and the momentum transfer from light to matter leads to a motion of objects that can be atom or larger scaled particle. Despite the pN magnitude of optical forces, the forces can locally alter the matter systems thus macroscopically modifying their mechanical and viscoelastic properties of the materials [1].

The momentum transfer must strictly obey the conservation laws in electromagnetics. In this section it will be shown that the formalism of Maxwell's stress tensor derived from the classic Maxwell's equations constitutes a conservation law for linear and angular momenta.

Conservation of Linear Momentum

Maxwell's Stress Tensor

Let us consider an illuminated arbitrary object immersed in vacuum. It is noted that in vacuum the linear momentum carried by a single photon is $p = \hbar\omega/c$. The formalism of Maxwell's stress tensor that constitutes the conservation of linear momentum can be expressed as

$$\int_{\boldsymbol{S}} \overleftrightarrow{\mathbf{T}} \cdot \mathbf{n}\mathrm{d}\boldsymbol{s} = \frac{\mathbf{d}}{\mathbf{d}\boldsymbol{t}}\frac{\mathbf{1}}{\boldsymbol{c^2}}\int_{\boldsymbol{V}}(\mathbf{E}\times\mathbf{H})\mathbf{d}\boldsymbol{V} + \int_{\boldsymbol{V}}(\boldsymbol{\rho}\mathbf{E} + \mathbf{J}\times\mathbf{B})\mathbf{d}\boldsymbol{V} = \frac{\mathbf{d}}{\mathbf{d}\boldsymbol{t}}(\mathbf{G_{field}} + \mathbf{G_{mech}}) \quad (1),$$

where Maxwell's stress tensor is

$$\overleftrightarrow{\boldsymbol{T}} = \varepsilon_0\boldsymbol{EE} + \mu_0\boldsymbol{HH} - \frac{1}{2}(\varepsilon_0|\boldsymbol{E}|^2 + \mu_0|\boldsymbol{H}|^2)\overleftrightarrow{\boldsymbol{I}} = \quad (2),$$

$$\begin{bmatrix} \varepsilon_0(E_x^2 - E^2/2) + \mu_0(H_x^2 - H^2/2) & \varepsilon_0 E_x E_y + \mu_0 H_x H_y & \varepsilon_0 E_x E_z + \mu_0 H_x H_z \\ \varepsilon_0 E_x E_y + \mu_0 H_x H_y & \varepsilon_0\left(E_y^2 - E^2/2\right) + \mu_0\left(H_y^2 - H^2/2\right) & \varepsilon_0 E_y E_z + \mu_0 H_y H_z \\ \varepsilon_0 E_x E_z + \mu_0 H_x H_z & \varepsilon_0 E_y E_z + \mu_0 H_y H_z & \varepsilon_0(E_z^2 - E^2/2) + \mu_0(H_z^2 - H^2/2) \end{bmatrix},$$

$\mathbf{n}$ is the normal outward direction to the closed surface S, $E^2 = E_x^2 + E_y^2 + E_z^2$ is the electric field strength, and $\overleftrightarrow{\mathbf{I}}$ denotes the unit tensor. Note that each term in Eq.1 has the unit of Newton. In Eq.1 the term at the far left side represents the momentum flux that propagates through the closed surface S while at the far right side $\mathbf{G}_{\text{field}}$ denotes the electromagnetic field momentum and $\mathbf{G}_{\text{mech}}$ is the mechanical momentum exerted on the arbitrary object inside the bound volume V in the exact form of Lorentz force equation. The conservation law represented by Eq.1 states that the linear momentum flux entering into the volume is used to exert optical force on the object inside that volume and the rest is carried in form of the field momentum. It is worth to remind that the object is assumed to be rigid in order to formulate Eq.1. To take into account the deformability of the object induced by the electromagnetic field, the electrostrictive and magnetostrictive forces are needed to be included in the derivation.

To calculate the net optical force exerted on the arbitrary object, one needs to evaluate the electric and magnetic fields on the closed surface S (depicted in Figure 1) as a result of light-matter interaction and then apply Eq.1.

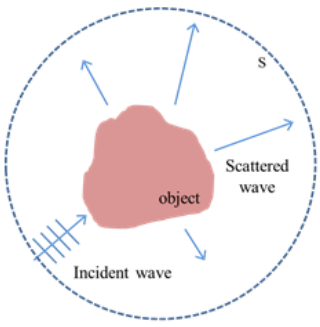

Figure 1 The optical force exerted on an arbitrary object is calculated by evaluating both incident and scattered fields at the enclosed surface S and then using Eq.1.

Now let us examine more general situation where an illuminated arbitrary object is submerged in a linear, isotropic, lossless, dispersionless, non-magnetic, and dielectric medium with refractive index n. In this situation, the question about the magnitude of electromagnetic momentum in dielectric media becomes nontrivial generating the Abraham-Minkowski controversy [2-12]. The controversy

centers around appropriateness of using Abraham ($p_A = \hbar\omega/nc$) and Minkowski ($p_M = n\hbar\omega/c$) formulations as the description of the linear momentum in dielectric media. Both theoretical considerations and experiments reported so far indicate that each form describes different electromagnetic quantities. Abraham momentum is a kinetic momentum of electromagnetic field while Minkowski momentum is a recoil momentum that is transferred to the object embedded in a dielectric medium. The momentum transfer and hence net optical force exerted on the object can be calculated using either Abraham or Minkowski formulations accompanied by an appropriate material counterpart and this should reach the same results. It is noted that the material counterpart can be understood as a momentum carried by atom inside surrounding medium and being transferred to the object.

The Maxwell's stress tensors in term of different forms of the linear momentum were discussed in Ref.[10]. The electromagnetic force is a consequence of the direct momentum transfer to the matter systems upon interacting with light. The optical force can be tuned to locally confine particle motion, drive its translational motion, and even form bound particle structures at microscopic scale. These manipulation modalities allow biophysicist to explore the microscopic world of biological systems and perform a variety of tasks including modifying, sorting, and transporting biological materials.

The theoretical and experimental aspects of optical trapping will be discussed next.

Optical Forces

Optical Trap

Since the pioneered work of single beam optical trap by Ashkin and his coworkers [13], the optical tweezer (OT) has become an important tool for research fields ranging from biology to soft condensed matter physics. The optical tweezer utilizes forces exerted by a tightly focused beam of light to stably trap microscopic objects. The basic working principle of OT is well understood for objects with size much larger than the wavelength of light. With the ray optic picture in mind, reflection and refraction of an incident ray after hitting the object alter the direction and magnitude of transmitted rays and

hence their linear momentum. This generates the momentum transfer which gives rise to the recoil optical force drawing the object toward the trapping site near the focus [14].

Conceptually, the OT can be modeled as a microscopic simple harmonic oscillator (see Figure 2). In this model the gradient forces, that serve as the restoring forces corresponding to a potential energy, are exerted to draw the object toward equilibrium trap center. The trapping site locates at a position where the balance between the gradient and scattering forces occurs. The gradient force is a conservative force, meaning that work done by the force field on the object for the movement in a closed path is zero. Its magnitude depends on the gradient of intensity. On the other hand the scattering force (also known as radiation pressure force) is a non-conservative force because light can do work on the object as it moves around in a closed trajectory in the vicinity of the trap. Its strength depends on the actual intensity, not the gradient. This force component tends to push the object out of the trap along the propagation direction of light.

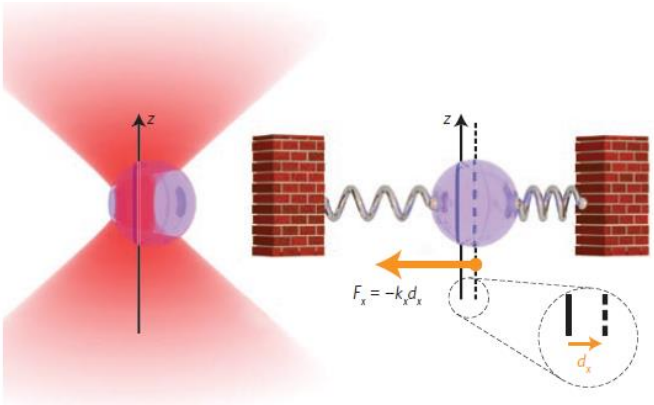

Figure 2 The simple harmonic oscillator model of single beam optical tweezer. Originally from ref.[15].

The stability of the optical trap is an important criterion to be carefully considered when designing new trapping geometry. In the context of this stability issue, an optical Earnshaw theorem states that a stable optical trap can't rely on only the scattering forces with the lack of the restoring forces even though there is a balance between different force components at one particular point [16].

The single beam optical trap can confine particle motion at one location at a time. Due to the advent of computer-controlled spatial light modulators (SLMs), multiple traps can be simultaneously formed by spatially modulating a phase pattern of laser beam and thus controlling intensity distribution at the objective's focal plane [17]. This holographic optical tweezer (HOT) technique finds novel applications in micromechanics, microfluidic, and fabrication.

Tunable Optical Forces

The field symmetry in a multi-body system can suggest the way how light mechanically interacts with matters. This should offer another accessible means to externally tune optical forces. To demonstrate the role of the symmetry on light-matter interactions, let us consider a simple situation in which a spherical particle is illuminated by a gradientless monochromatic plane wave. Upon interacting with light, the dissipation (scattering and absorption) process reduces the total photon linear momentum along the incident wave propagation and as a consequence of conservation of linear momentum, the particle is pushed by radiation pressure forces. There is no net momentum transfer along the transverse direction with the beam propagation and thus lateral particle motion because of the mirror symmetry of the scattering of light. In other words, the intensity distribution of the scattered light is cylindrically symmetric along the incident direction. To break the symmetry results in a transverse component of optical forces that displaces the particle laterally. The symmetry breaking can be achieved through the modification of the manipulated particle, environment, or incident radiation. The particles can be structured to possess cylindrically asymmetric shape or optical properties. As a result of light scattering of particles, the cylindrically asymmetric scattering phase functions of the particles (defined in Ref. [18]) give rise to the lateral component of optical forces.

The effect of the symmetry breaking on optical forces can be seen in another situation in which strongly focused Gaussian beam illuminates an off-axis spherical particle. Due to the symmetry breaking of light scattering along the transverse direction, the lateral component of trapping forces is

exerted on the particle. Now it is shown that the symmetry of electromagnetic fields plays a key role in tailoring the optomechanical interaction.

The challenging question is whether breaking the field symmetry can be employed to drive unusual dynamics of microscopic objects. The clear answer for this question will be given in Chapter 2. Next, can gradientless light be used to counterintuitively attract objects towards a light source? To answer it, let us examine a simple situation in which a nonabsorbing scattering object ("black box") is exposed by gradientless plane waves at an angle θ with respect to the z axis. This "black box" ideally converts all incident plane waves from different propagating directions into scattered waves along the z axis. As a result of the momentum conservation, the "black box" is counterintuitively pulled against the flow of light. The schematic diagram of the "black box" system is depicted in Figure 3. Although the situation seems unrealistic, but it shows that optical pulling force can be realized with the necessity of nonparaxial illumination and enhanced forward scattering of objects. This is again a direct consequence of symmetry breaking of angular distribution of scattered light.

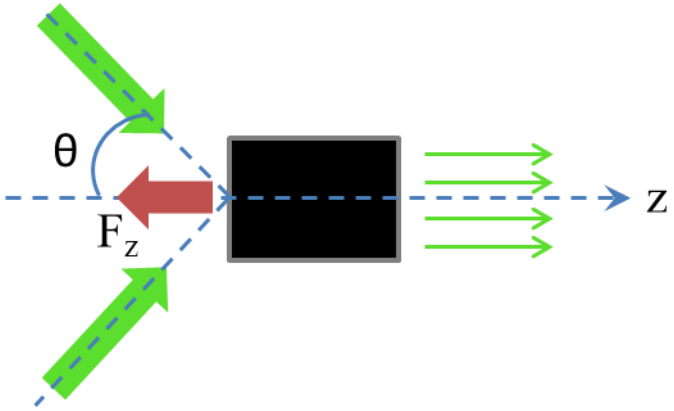

Figure 3 The "black box" which converts all incident plane waves at grazing angle θ into scattered waves along the z axis is pulled against the flow of light due to the increase in the photon linear momentum along the z direction.

To implement the concept illustrated in Figure 3, it was theoretically proposed that a propagation invariant Bessel beam can exert optical pulling force on spherical particles over a large interaction length within certain conditions of structural parameters and illumination [19]. In specific parameter spaces, the constructive interference of induced radiation multipoles simultaneously excited

(Scattering theory of small particles can be found in [18].) gives rise to dominant forward scattering and hence negative optical scattering force. It is worth to note that the use of a Bessel beam reduces input linear momentum due to the fact that a beam is a superposition of plane-wave components whose propagating vectors form a cone at an angle θ with the propagation axis. The optical pulling effect can be also realized on submicron semiconductor particles that can emit only electric and magnetic dipolar radiation without significant loss in near-infrared regime [20, 21]. Recently, the theoretical predictions have been experimentally validated and optical transport and sorting of submicron particles were also demonstrated using polarization dependence of optical forces [22].

The concept of negative forces can be extended to manipulate a multiply scattering, nonabsorbing object with arbitrary shape and size through the complete control of phase and polarization of individual plane waves constituting an incident beam [23]. The optimization of phase and polarization can be performed to enhance forward scattering resulting in optical forces pulling the entire object against the photon stream. This wavefront shaping is known as a technique for imaging and focusing in strongly scattering media as well [24]. The proof of concept experiment was conducted in acoustic domain [25].

There are other different schemes developed to reverse the direction of optical forces as concisely reviewed in ref.[26].

Conservation of Angular Momentum

The Orbital and Spin Angular Momentum of Light

Light carries not only linear momentum but also angular momentum. In 1936, Beth demonstrated a rotation of a birefringent waveplate illuminated by circularly polarized light [27]. This is a mechanical consequence of direct transfer of spin angular momentum (SAM) from a light beam to matter. The SAM is associated with the state of polarization of light. This part of the total angular momentum is intrinsic meaning that it doesn’t depend on the choice of calculation axis.

Later, Allen *et al.* found that optical beams with an azimuthal phase distribution in form of $\exp(im\phi)$ carry an orbital angular momentum (OAM) that is the cross product of the position vector (**r**) and linear momentum density (**p**) [28]. It is noted that the magnitude and sign of the integer *m* indicate the number of intertwined helices of wavefront and the handedness, respectively. The OAM relates to helical phase front but polarization. In general, there are both intrinsic and extrinsic OAM depending on the symmetry of apertured field distribution with respect to the beam axis [29].

The distinction between spin and orbital angular momenta can give rise to different nature of light-matter interaction.

Optical Micromanipulation Based on OAM and SAM

The exchange of angular momentum from light to microscopic objects drives them to rotate in orbit and/or around themselves [30]. The momentum transfer can be induced by different mechanisms. The transformation of the polarization state upon interacting with a birefringent particle leads to the SAM transfer and hence spinning around its own particle axis [31]. This is the microscopic analog of Beth's original experiment. The OAM transfer induced by the transformation of the laser mode [32, 33] can give rise to the rotation of particles in orbit. One way to understand angular motion of particles is that the linear momentum flow in the azimuthal direction creates optical forces pushing particles along circular trajectory.

Another significant work was to demonstrate the mechanical equivalence of spin and orbital angular momentum of light on trapped absorbing particles [34]. The circularly polarized Laguerre-Gaussian beam with $m = 1$, $\sigma = 1$ induces the rotational motion of the particles with the total angular momentum of 2ħ per photon. After switching into the opposite handedness of the polarization state, the particles stopped rotating completely with the zero total angular momentum. This confirms that the helical phased beam with the integer *m* possesses the discrete OAM of mħ, the same unit as the spin component.

Optical micromanipulation based on SAM and OAM of light can be employed to study hydrodynamic interaction, sense fluid properties, and control fluid flow at microscopic level. In Ref.[35] two birefringent particles were excited by two circularly polarized beams with opposite handedness, forming the microfluidic pump used for regulating fluid flow. The flow can assist in transporting and sorting microscopic matter on microfluidic lab-on-chip platforms.

Throughout this section, one may think the transfers of the OAM and SAM from light to matter are two independent processes. In fact, it isn't true and the conversion between two components of AM can occur during fundamental processes of reflection-transmission [36] and scattering [37]. The weak spin-orbit coupling can result in a shift of a centroid of an electromagnetic beam [38]. All of reported works showed the effect on dynamics of electromagnetic beam (briefly discussed in Chapter 4) but matter. In Chapter 2 we will demonstrate the concept of optical force exerted on matter as a manifestation of the spin-orbit interaction. The unusual behavior of optical force involves the breaking of field symmetry at dielectric interface.

CHAPTER 2: BREAKING SYMMETRIES IN COMPLEX ELECTROMAGNETIC FIELDS

Scattering is a fundamental process in which the redistribution of electromagnetic field occurs upon interacting with matter. The scattering pattern suggests the way how light mechanically exerts forces on objects. As been described in Chapter 1, the pushing-pulling action of light can be achieved by manipulating the angular intensity distribution of light waves along the incident beam direction. To gain a complete optical control on colloidal dynamics, the condition for generating lateral forces has been recently examined [39]. Besides shaping objects, the incident wave can be structured to create asymmetric light scattering pattern along the transverse direction. As a result of momentum transfer, light can laterally act on objects.

The framework of field symmetry and conservation laws can be employed to not only manipulate matter but also explore dynamic aspect of quantum phenomena. In the first part of Chapter 2, optical situation was implemented to demonstrate the existence of optical forces acting back on a vortex formed by scattering of spheres by circularly polarized light. The detection of forces in the optical setting should assist in interpreting the interaction and its mechanical effect in the original Aharonov-Bohm effect. It is worth to note that the occurrence of unusual component of optical forces can be explained by either a shift of a centroid of a scattering pattern or an asymmetric scattering phase function. Both of approaches associated with conservation of momentum will be stated clearly.

Now the general description of the original Aharonov-Bohm effect will be introduced along with relevant works.

Forces in an Optical Analog of Aharonov-Bohm Effect

Introduction to the Aharonov-Bohm Effect

In the original Aharonov-Bohm (AB) setting, a magnetic vector potential forms a vortex that interacts with an electronic waveform to generate a typical interference. The matter wave feels the nonlocal presence of the magnetic field through its associated vector potential. In terms of the phase

difference accumulated between the two parts of a wave, the topology of the electron wave function corresponds to the strength of wave-front dislocation [40].

Phenomena related to the original AB effect have also purely classical analogs where wave interference leads to interaction forces between quasiparticles and vortices [41, 42]. An AB-like waveform can also be imparted to classical waves in moving media [43, 44] where flows play the effective role of vector potentials [45]. Because of the related phase gradients, an exchange of momentum is established between wave and fluid. This circumstance is part of a larger argument around the fact that only some aspects of the AB phenomenon have classical analogues [45-47].

Nevertheless, optical analogs of AB effect have also been proposed and demonstrated. Experiments interpreted as manifestation of AB phenomena were concerned with both linear and nonlinear wave-front splitting by velocity vortex fields [48] as well as with the creation of effective gauge potentials for photons by harmonically modulating the refractive index of different photonic systems [49, 50]. Notably, it was also shown, that even in the paraxial regime of propagation, the use of anisotropic [51] and optically active media [52] leads to cumulative effects that reproduce the characteristics of AB phase change. A mechanism for photonic AB caging in waveguide or couples-resonator lattices has also been suggested [53]. Recently, a photonic AB effect was also demonstrated where the nonreciprocal phase was created via photon–phonon interaction [50]. In a fascinating experiment, the scattering circularly polarized wave on a subwavelength hole [54] reproduced the typical AB phase change for the case of plasmonic waves. Creating such optical equivalents permitted researchers to illustrate in a convenient way and at macroscopic scales some of the fundamental quantum mechanical phenomena.

In spite of the vast literature on the subject, arguments regarding the associated dynamics are still unsettled because of the possible dual interpretation of typical interferometric observables in AB experiments. The quantum mechanical formulation describes how a charged matter wave accumulates a path-dependent phase that is determined by the effective vector potential throughout the space

accessible to the particle [55]. The interferometric observables however can also be described as the result of a Lorentz force acting classically on charged particles [56].

Notably, in the context of momentum exchange, the fact that the moments of spatial distribution of intensity in the interference pattern do not depend on the accumulated phase – the so-called "no shift theorem" [57] – was interpreted as the absence of momentum transfer in AB experiments [58]. However, this "no shift theorem" is violated for finite size wave-packets with nonzero intensity at the magnetic flux line [59]. This means that the issue of observable forces cannot be approached in the traditional AB setting involving infinitely extended plane waves. On the other hand, when a wave-packet or a beam is considered, the notion of trajectory or shift of a center of mass can be invoked as in Shelankov's original paraxial analysis [58]. A similar argument has been raised by Berry when suggesting that a beam's deflection by a step mirror constitutes, in fact, an optical analog of the AB phenomenon [59]. Thus, in classical wave optics experiments, by following the evolution of the center of mass of a wave-packet or a beam, one can probe the forces arising in AB settings. Here we create an optical situation that permits observing experimentally such reaction forces that appear as a result of conservation of the canonical momentum. We will show that electromagnetic scattering by a small sphere can be manipulated in such a way that a change in the center of mass of the scattered intensity determines the appearance of specific, measurable forces. This constitutes the first experimental demonstration of the dynamic consequences of phase dislocations at a vortex state leading to nondissipative mechanical forces.

Optical Setting

First, we describe our Aharonov-Bohm optical setting and provide theoretical validation for appearance of forces. When a circularly polarized plane wave $\mathbf{E}_1$ is incident on a spherical scatterer as shown in Figure 4a, a vortex field distribution $\mathbf{E}_1^s$ emerges (Figure 4b) centered at the location of the scatterer [60]:

$$\boldsymbol{E}_1^s \propto \boldsymbol{E}_1\left[S_2\widehat{\boldsymbol{\theta}} + iS_1\widehat{\boldsymbol{\phi}}\right]\boldsymbol{e}^{i\boldsymbol{\phi}}. \tag{3}$$

Here $S_1(\theta,\phi)$ and $S_2(\theta,\phi)$ are the components of scattering matrix for scattering direction (θ,ϕ) (see Figure 4a) while $\hat{\theta}$ and $\hat{\phi}$ are the local orthogonal unit vectors of spherical coordinate system. The physical origin of this vortex field is the partial transformation of spin to orbital angular momentum during the wave interaction with the scatterer [60]. We note that the phase distribution of scattered field $\mathbf{E}_1^s$ is similar to the phase $\psi^s = \psi_0 e^{im\phi}$ accumulated by an electronic plane wave ψ_0 interacting with a hypothetical magnetic monopole [61] with charge *m*. In the case of the electron, the phase dislocation can be observed interferometrically by splitting the wave and then recombining it.

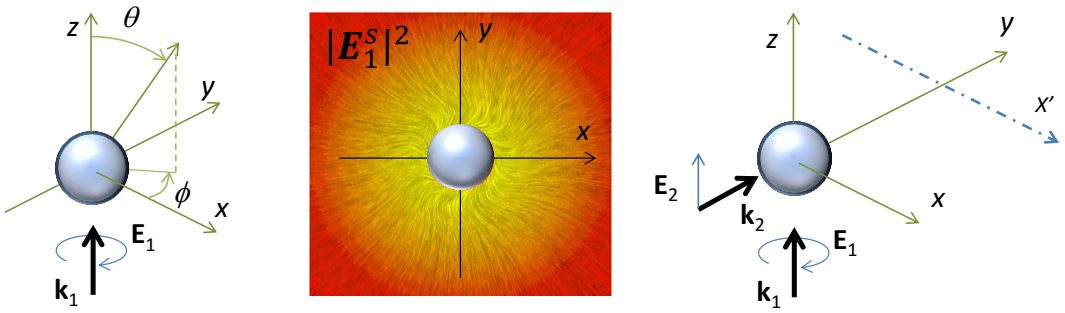

(a) (b) (c)

Figure 4 Optical setting: vortex generation by scattering on a spherical particle. (a) Spherical particle illuminated by a circularly polarized plane wave with electric field strength $\mathbf{E_1}$ and wavevector $\mathbf{k_1}$; (b) The power flow in the plane z=0 clearly demonstrates the vortex structure; (c) A second, linearly polarized wave $\mathbf{E_2}$ provides the interferometric reference.

The vortex field $\mathbf{E}_1^s$ can also be "probed" interferometrically using a reference, plane wave $\mathbf{E}_2$ linearly polarized along *z* and propagating along the y-axis as shown in Figure 4c. This is similar to the situation discussed previously for plasmonic waves interference [54] that manifest wavefront dislocations typical to AB effect.

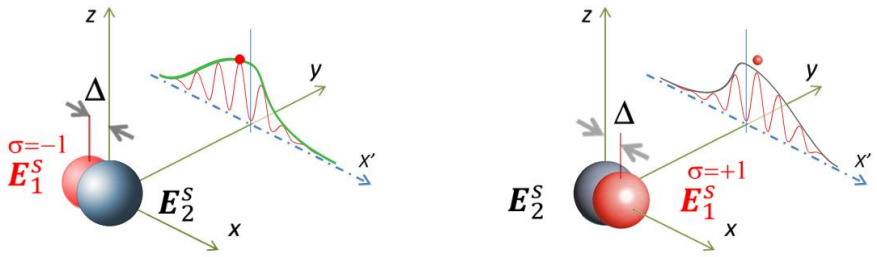

(a) (b)

Figure 5 Effective interference leading to changes in the wave's momentum density. Due to the transformation of angular momentum during scattering of circularly polarized light on a spherical object (gray), when seen from the far-field the sphere appears at a shifted virtual location (smaller red sphere). This shift in the apparent location **Δ** depends on the spin of the incident wave: (a) $\boldsymbol{\sigma = -1}$; (b) $\boldsymbol{\sigma = +1}$. The corresponding maximum of interference pattern (indicated by a small red dot) is shifted to the left or to the right with respect to the symmetry point depending on the helicity of incident wave.

Let us examine now the total scattered field in the (x',z) plane (Figure 5). The scattered field $\mathbf{E}_2^s$ is still linearly polarized while $\mathbf{E}_1^s$ is, in general, elliptically polarized maintaining the helicity of $\mathbf{E}_1$. The result of their interference can be interpreted as shown schematically in Figure 5.

Seen from a distant observation point, the vortex field $\mathbf{E}_1^s$ appears to originate from a virtual location shifted by Δ with respect to the origin of coordinates [37]. Thus, the intensity distribution observed along a direction x' is

$$I(x') \propto \left|\boldsymbol{A}_1(x', \Delta)e^{i\sigma\phi} + \boldsymbol{A}_2(x')\right|^2 \qquad (4),$$

where the functions $\mathbf{A}_1$ and $\mathbf{A}_2$ describe the field variations as determined by the corresponding scattering phase functions, ϕ is an additional geometric phase due to the vortex field while $\sigma = \pm 1$ is the topological charge of the field resulting from the scattering of a circularly polarized plane wave by a sphere. Note that Δ changes to $-\Delta$ when the spin σ of $\mathbf{E}_1$ flips and, consequently, the vorticity of $\mathbf{E}_1^s$ changes [37] as illustrated in Figure 5. Thus, the modulated intensity pattern should move left or right with changing the handedness of illumination light.

The interference between the two waves is analog to the formal solution of Schrödinger's equation for a plane wave in the circular gauge $\exp\{i(\boldsymbol{k}.\boldsymbol{r} + \phi)\}$ [59]. In our case, the second wave $\mathbf{E}_2^s$

introduces the necessary scattering directionality and also it imposes a finite range of accessible scattering angles. Thus, this second wave serves the role to limit the width of the wave-packet in the Aharonov-Bohm setting [59]. Taking also into account the fact that $\mathbf{E}_2^s$ has nonzero intensity at the vortex location, we can expect the deflection of the scattered pattern $|\mathbf{E}_1^s + \mathbf{E}_2^s|^2$, as this is analogous to the conditions assuring the shift of the beam diffracted by magnetic flux line [59].

Note that in our description the fields $\mathbf{E}_1$ and $\mathbf{E}_2$ are coherent. Their phase relationship is equivalent to an initially non constant phase across the wave-packet in the AB setting, which does not influence the way in which the phase accumulates around the vortex.

To inspect the mechanical consequences, one can invoke the *actio et reactio* principle. The time-averaged radiation force, F_{AB}, acting on the center of mass of the sphere is equal in magnitude, and opposite in sign, to the rate of change of momentum of the electromagnetic field. Thus, in the example discussed here the "center of mass" of intensity shifts from $x' = 0$ position (Figure 5)

$$\int x' I(x') dx' \neq 0 \tag{5}$$

and it also depends on Δ, meaning that a force $F_{AB} \equiv F_x$ should act on the particle with a sign depending of fields' vorticity. Indeed, the force acting on the particle can be expressed in terms of the scattered fields as [23, 62]

$$F_x = -\frac{\varepsilon_0 r^2}{2} \int_\Omega \left| \boldsymbol{A}_1(\hat{\mathbf{r}}, \Delta) e^{i\sigma\phi} + \boldsymbol{A}_2(\hat{\mathbf{r}}) \right|^2 \hat{r}_x d\Omega \tag{6},$$

where $\hat{\mathbf{r}}$ is a unit vector corresponding to angle of integration Ω and $\hat{r}_x$ is its projection onto x axis, r is the radius of the integration sphere. The integration in Eq. (*6*) is performed over a solid angle of 4π steradians. Because of the symmetry properties of the scattering phase functions in the case of scattering from a sphere, Eq.(*6*) can be rewritten as

$$F_x = -\varepsilon_0 r^2 \int_\Omega Re\left[\boldsymbol{A}_1(\hat{\mathbf{r}}, \Delta) e^{i\sigma\phi} \boldsymbol{A}_2^*(\hat{\mathbf{r}}) \right] \hat{r}_x d\Omega \tag{7}.$$

In this form, one can easily see that the acting force F_{AB} depends on the spin of the incident wave: $F_x(\sigma = 1) = -F_x(\sigma = -1)$. Let us stress again that force F_{AB} depends only on scattered fields and, thus, is nonconservative force. Also, there are no other gradient or radiation pressure forces acting in *x* direction.

We would like to draw the attention to the close similarity between the expressions in Eqs. (*5*) and (*6*). By expressing the x-component of the force directly in terms of the scattered fields provides a simple and clear description of the dynamics associated with this AB setting, as determined by the conservation of canonical momentum.

Another interesting observation can be derived from Eq. (*6*). As a result of the angular integration, the resultant transversal force is zero when the scattering phase functions are isotropic because the shifts of the interference patterns cancel in the forward and backward directions. This is exactly what happens in the particular case of scattering from a dipole, a situation that can also be confirmed by simple electromagnetic calculations. Nevertheless, the scattering from any finite size particle is always anisotropic with respect to forward-backward directions leading to a nonzero AB force (Figure 6).

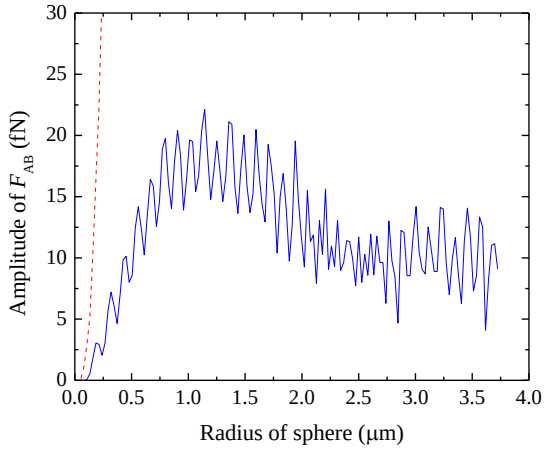

Figure 6 Amplitude of transversal force $\boldsymbol{F_{AB}}$ as a function of particle size. The forces are calculated directly from Mie scattering phase functions according to Eq. (**6**). Calculations were performed for a polystyrene sphere with refractive index 1.6 in water which is illuminated with radiation of 532nm wavelength from a 50mW beam power focused into a 10μm

radius spot. The magnitude of the transversal force (solid blue curve) is much smaller than the corresponding radiation pressure (red dashed curve), which makes the $\boldsymbol{F_{AB}}$ detection challenging.

The occurrence of an AB force transversally acting on a Mie sized particle can be understood within the symmetry consideration. In this point of view the role of two incident beams and a spherical particle will be clarified. The scattering of a circularly polarized wave creates a vortex field centred at the location of the particle because of a partial transformation from spin to orbital angular momentum. The spiraling of the energy flow illustrated in Figure 7 breaks the mirror symmetry of the light scattering. Then an illumination of a linearly polarized wave further breaks its center symmetry. At the far field the energy flow corresponds to the propagation direction that relates to the linear momentum of light. Hence the symmetry breaking in the flow pattern induced by the superposition of two incoming waves enables linear momentum transfer from light to matter driving transversal motion of the particle along x-axis. It is worth to note that the characteristics and direction of this force component are different from those of radiation pressure forces acting along the propagation directions of two incident waves (y and z-axes).

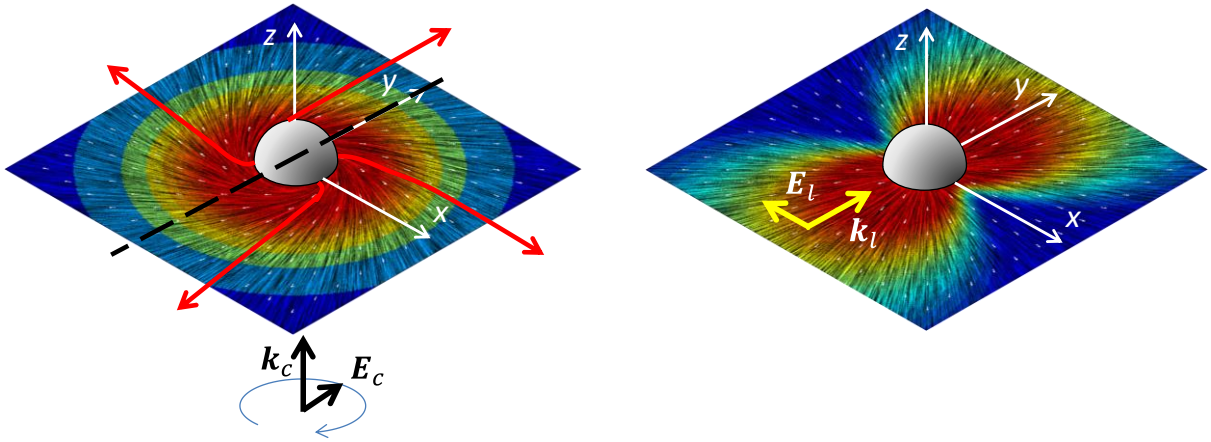

(a) (b)

Figure 7 Symmetry breaking in energy flow patterns upon illuminating a spherical particle with (a) a circularly or (b) linearly polarized wave along propagating directions, $\boldsymbol{k}_c$ and $\boldsymbol{k}_l$, respectively. Poynting vector field lines shown in both patterns were calculated by using Mie theory. Red arrows were inserted into (a) only to illustrate symmetry breaking and necessary conditions for generating transversal force along x direction. The color represents the intensity distribution.

Experimental Demonstration

The practical implementation of the concept is more involved. First of all, the linearly polarized plane wave provides a fixed phase reference for the interference. Because the force F_x in Eq. (*7*) depends on the relative phase between the complex amplitudes $\mathbf{A}_1$ and $\mathbf{A}_2$, the magnitude of the transversal force will oscillate accordingly. In particular, if the phase between $\mathbf{A}_1$ and $\mathbf{A}_2$ is changed by π, the force changes its sign that immediately follows from Eq.(*7*). Practically, this means that the force F_x acting on a spherical particle will depend on its position in the plane (*y*,*z*). This is a direct consequence of the optical setting necessary to observe the AB force: the asymmetric phase of a scattered wave has to be generated by a mobile element whose displacement can be followed. Second, the magnitude of F_{AB} is rather small (compared, for example, to radiation pressure) and does not steadily rise with an increase of particle size as can be seen in Figure 6. The further growth is prevented by the spatially oscillatory nature of the transversal force that complicates the experimental detection of the force. The oscillations of the force amplitude visible in Figure 6 are determined by the way the particle covers the F_{AB} oscillation period.

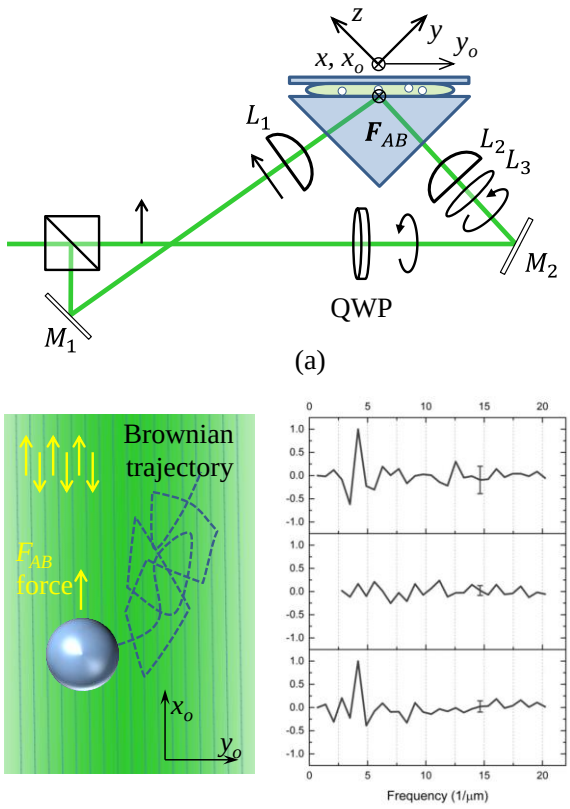

Figure 8 Experimental verification of the existence of transversal force. (a) Experimental setup for observing transversal F_{AB} forces. (b) Schematics of the periodic behavior of F_{AB} forces acting on a particle in the observation plane. The particles trajectories are also influenced by overwhelming Brownian motion. (c) The amplitude of reconstructed periodic motion (with noise subtracted) as a function of spatial frequency for combinations of circular and linear polarized waves (top and bottom panels) and for a combination of two linearly polarized waves (center panel).

Experimentally, 2μm diameter polystyrene particles were suspended in water and exposed to two overlapping coherent beams as shown in Figure 8a. A combination of rotating waveplates allows setting linear and circular polarizations for the incident field. The two beams were always orthogonally polarized and create a uniform intensity distribution. The particles were pushed by radiation pressure against upper cover slip that served as an observation plane. Besides radiation pressure, the particles are also subjected to transversal F_{AB} forces acting along the x axis as discussed above. Because the relative phases of two beams change in the observation plane, the magnitude and direction of the force varies like $F_{AB} \propto \cos\left(\sqrt{2}ky_0 + \delta\right)$ (Figure 8b). Even though each particle occupies several oscillation periods of F_{AB} (approximately 282 nm each for incident field wavelength

532 nm), the overall transversal force is not zero as seen in Figure 6. The particles were imaged onto a CMOS camera and their trajectories were recoded and further processed to evaluate the effect of transversal forces. During the experiment, the action of random Brownian forces impeded the direct observation of spatially periodic force F_{AB}.

The results for the recovered spatial frequencies of particles' displacements Δx_0 along direction y_0 are summarized in Figure 8c. The upper and lower panels correspond to circularly polarized $\mathbf{E}_1$ with spin $\sigma = \pm 1$ and a clear peak is visible corresponding to a spatial frequency 3.6 μm^{-1} (period 280nm). This agrees very well with the predicted oscillation period of 282 nm for the transversal F_{AB} forces. Under a linear polarization on the other hand (middle panel), a purely isotropic motion is observed indicating the absence of any transversal forces.

Concluding Remarks

Aside from being the first direct measurement of dynamical manifestation of the field vortex, this demonstration has several important implications. First of all, the question of forces in general and those acting in various AB settings in particular is of fundamental interest in formulating the laws of physics. On one hand, within the accuracy of a semiclassical description, the momentum density of the wave does not change during the AB interaction and, according to the principle of *actio et reactio* one would not expect that the wave exerts any force back onto the vortex. However, this argument does not necessarily apply when the phase gradient represents the true momentum and the conservation laws must be carefully examined.

Newton's second law has been quite successful in the Hamiltonian description of optics. The conservation of canonical momentum, the equivalent of the third law, however, still raises questions for systems out of equilibrium. Optical experiments such as ours permit simultaneous measurements on the field and the particles and can therefore examine the role of conservation laws and symmetries in complex interacting systems.

The non-trivial dynamics that can be controlled in our optical setting has implications for a broad range of phenomena where forces act on vortex fields and where experiments are almost inexistent or difficult to conceive. For instance, our results may impact the understanding of gravitational AB effect where particles are scattered by a spinning cosmic string moving in the background matter [46] or the so-called Iordanskii force acting on a vortex moving in superfluids [63].

Our experiment also represents a direct demonstration of dynamics driven by nonconservative curl forces, for which there is no associated scalar potential [64]. The motion of a charge in the field of a magnetic monopole is a typical example of this class of dynamical phenomena, which are essentially untested.

Finally, we anticipate that the dynamical system studied here may offer insights into concepts such mechanical action and non-locality and it may also stimulate interest in other novel phenomena in photonic systems that are analogous to charges coupled to magnetic fields.

So far in this chapter optical setting was created to explore dynamic aspect of the Aharonov-Bohm effect. The existence of an experimentally detected AB force can be considered as a consequence of a shift of a centroid of a scattering pattern according to conservation of momentum. In addition, the framework of symmetry was introduced to suggest the behavior of optical forces without full electromagnetic calculation. In this way of thinking it appears that the AB force occurs due to symmetry breaking of the light scattering induced by complex illumination.

Throughout the dissertation, the framework of symmetry becomes a useful tool for engineering unusual component of optical force with unique characteristics paving new ways in optical manipulation of matter. In the remaining part of this chapter, it will be theoretically and experimentally demonstrated that unstructured light can exert lateral forces on microscopic particles with isotropic shape and optical properties floating on liquid surface owing to symmetry breaking of the light scattering, similar to the origin of AB force. Here the presence of dielectric interface plays a crucial role in breaking the field symmetry around the isotropic particle.

Mechanical Action of Optical Spin-Orbit Interaction

Earlier an incident electromagnetic field is structured to tailor scattering phase function upon interacting with matter. This, in turn, leads to a control over the force field distribution determined by Maxwell's stress tensor. Now it will be shown that the optomechanical effect can be alternatively controlled by modifying environment surrounding matter with unstructured light. It permits manipulating matter in a robust manner even at low dimensional level.

Firstly, let us briefly describe the nature of optical forces under our investigation. The new type of optical force appears because of the exchange between two different components of momentum. To be more specific it is a momentum transfer from spin angular momentum of incident light to orbital angular momentum of scattered one. This polarization dependent optical force is different from usual component of radiation pressure and torque. It acts perpendicularly to the direction of light propagation. It should be noted that the mechanical effect during spin-orbit transformations was previously predicted in light reflection and refraction (spin-Hall effect of light) [65].

As being an origin, the new mode of mechanical action can be regarded as a result of symmetry breaking of light scattering during optical spin-orbit interaction affected by the presence of nearby interfaces. To understand this quantitatively, let us consider a spherical, dipole-like particle with a radius equal to approximately $1/10^{th}$ of the wavelength. The particle is located at the interface of two media with different refractive indices and is illuminated by a circularly polarized wave as shown in Figure 9a. The distribution of intensity and the power flow (time-averaged Poynting vector) in a plane *yz* perpendicular to the plane of incidence is shown in Figure 9b. As can be seen, the spiraling of energy flow breaks the mirror symmetry of the light scattering. Because of the optical spin Hall effect that arises from partial momentum transformation in spherical geometry [37], light to the left of the $y = 0$ plane propagates mostly in the upper medium while the opposite happens at the right side of the particle. The presence of the interface further breaks the central symmetry of the light distribution. As the magnitude of wave's momentum is determined by the properties of medium it propagates

through [66], this scattering asymmetry unbalances the transversal linear momentum. Consequently, a side force perpendicular to the original wave propagation should act on the particle with a magnitude determined by its scattering phase-function [62]. We will further elaborate this idea analytically and confirm it by exact numerical calculations and by experimental results.

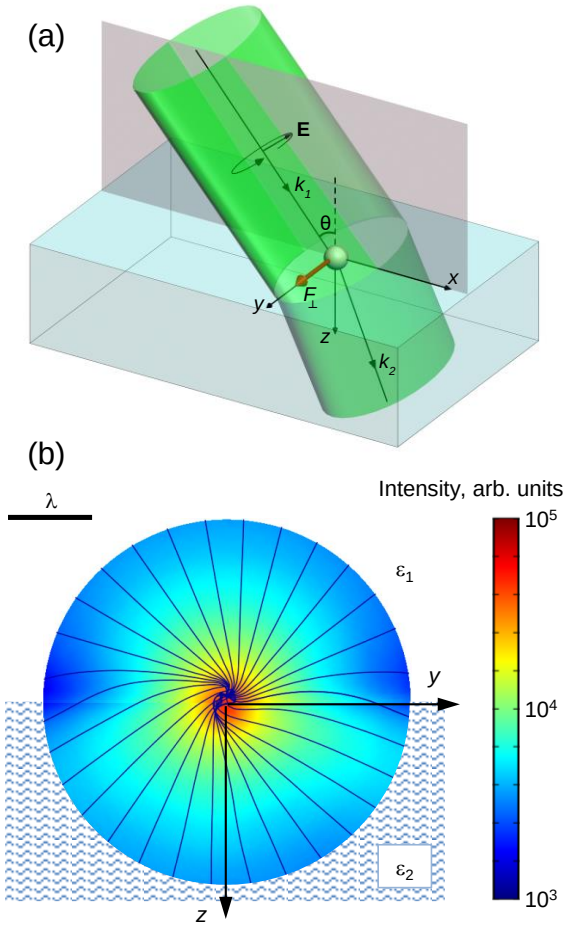

Figure 9 Scattering of circularly polarized light off a spherical particle located at the interface between two dielectric media. (a) Illumination geometry: a circularly polarized beam is incident along *xz* plane. (b) Distributions of intensity (color map) and power flow, Poynting vector, (lines) in the plane *yz* perpendicular to the plane of incidence *xz*. Calculations (Comsol Multiphysics) were performed for a 100nm TiO_2 particle placed at water-air interface with dielectric permittivities of $\boldsymbol{\varepsilon_1}$ =1 and $\boldsymbol{\varepsilon_2}$ =1.77. The particle was illuminated by a circularly polarized wave with the wavelength of λ=532nm incident at 55°.

Analytical Formulation for Dipole Sized Particles

If a dipolar particle is located entirely inside one of the media, the problem can be solved analytically. In the first example, we consider a point dipole located a distance z_0 away from the interface between two semi-infinite transparent media 1 and 2. The dipole **d** is placed in the lower medium 2 and a circularly polarized plane wave of amplitude E_{0I} is incident from the upper medium

1. We are interested in the force $F_\perp$ acting on the dipole in a direction perpendicular to the plane of incidence xz (Figure 9a). This force can be found by integrating the scattering phase function over 4π solid angle or by integrating the Maxwell's stress tensor over a closed surface surrounding particle. An asymmetric field distribution would ensure that these integrals are nonzero. In the case of dipole, however, one can follow a much simpler approach derived directly from the Lorentz force formulation and find the force to be [67]

$$F_\perp = \frac{1}{2} Re\left(\boldsymbol{d}\partial_y \boldsymbol{E}^*\right) \quad (8),$$

where **E** is the local field at the location of the dipole. The symbol ∂_y denotes partial derivative with respect to transversal coordinate y (Figure 9a). The field **E** represents the superposition of the transmitted field $\mathbf{E}_T$ and the dipolar radiation $\mathbf{E}_d$ scattered from the interface back to the dipole. Obviously, $F_\perp$ is zero for a normal incidence $\theta_I = 0°$ because of the azimuthal symmetry of the field. The force tends also to zero for grazing angles of incidence $\theta_I \to 90°$ when no light reaches the dipole inside the medium 2. Because of spin-orbit transformations at intermediate angles of incidence, $\mathbf{E}_d$ lacks symmetry with respect to $y = 0$ plane and, consequently, its *y*-derivative is nonzero. In these conditions, the transversal force becomes

$$F_\perp = \frac{k^2}{\varepsilon_0} \mathrm{Im}\left(d_y d_z^*\right) \mathrm{Im}(\partial_y G_{yz}^0),$$

$$\partial_y G_{yz}^0 = \frac{1}{8\pi k_2^2} \int_0^\infty r_p\left(k_\rho\right) k_\rho^3 \, exp(2ik_{2z}z_0)\, dk_\rho \quad (9).$$

Here $G_{yz}^0 = G_{yz}(\mathbf{r}_0, \mathbf{r}_0)$ is the yz component of the Green's function tensor [68], r_p is the amplitude reflection coefficient for *p*-polarized wave, k_2 is the wavenumber in medium 2, $k_{2z} = \sqrt{k_2^2 - k_\rho^2}$, k is the wavenumber in vacuum, and ε_0 is vacuum dielectric permittivity. We must stress that because there are no variations of intensity along the surface, Eq.(*9*) describes a purely nonconservative force. Furthermore, one can see that the force is determined by two factors: the first one is specified by

configuration of the field in the vicinity of interface, the second one is entirely determined by the material properties of two media.

When examining Eq.(*9*) one can see that the force is nonzero only if there is a phase difference between the transversal components *y* and *z* of dipole momentum. This practically means that transversal force exists only for elliptically polarized light and disappears in the case of linearly polarized wave. It also follows that this force changes sign with the change of the helicity of incident wave.

For the case of a dipole placed close to the surface ($z_0 \to 0$) one can obtain an explicit expression for the transversal force. It is interesting to notice that even though the electrostatic approximation can be used to calculate dipole moments for $k_2 z_0 \ll 1$, it is unsuitable for evaluating our transversal nonconservative force. The electrostatic approximation does not include retardation effects (field phases) and, thus, can account only for conservative forces. This demonstrates that the electrostatic approximation imposes even more severe limitations than previously believed.

For a dipole far from the interface ($k_2 z_0 \gg 1$), the integral in Eq.(*9*) can be evaluated asymptotically to obtain

$$F_\perp(z_0 \to \infty) \sim \frac{k_2^4}{4\pi\varepsilon_2\varepsilon_0} Im\left(d_y d_z^*\right) \frac{sin(2k_2 z_0)}{(2k_2 z_0)^2} \frac{n_{12}-1}{n_{12}+1} \qquad (10).$$

The presence of reflection coefficient $n_{12} - 1/n_{12} + 1$ factor in Eq.(*10*) suggests another interpretation of the transversal force for particles located far from interface. The vortex spherical wave created by the dipole is reflected from the interface and causes a back-influence on the dipole itself. The force can be understood then as originating from the phase of this vortex. The same phase, for example, makes particles orbiting in vortex beams [31]. In our case the particle drags vortex with itself creating a self-propelling linear motion. This interpretation becomes somewhat similar to the one suggested for chiral particles at an interface [69]. However, our demonstration indicates that this phenomenon is more general and does not necessarily rely on exotic material properties.

The oscillating behavior of $F_\perp$ with distance z_0 resembles the one occurring in optical binding when optically bound particles are illuminated with circularly polarized light [70]. However, the distance-dependent force in that case decayed faster [70] than the force in Eq.(*10*).

In a similar way one can estimate transversal force for a particle located in the same medium as incident wave. This case may be more favorable in terms of the magnitude of the lateral force: it can be comparable to the radiation pressure. However, one should be careful in interpreting the nature of this transversal force: the force in Eq.(*9*) should be distinguished from the action of a transversal spin momentum that can appears during the interference of incident and reflected waves [71-73]. Because the spin momentum does not affect dipolar particles, its detection requires the presence of multipoles. This type of transversal force was detected recently in an Aharonov-Bohm optical setting [39]. As opposed to the force due to spin momentum, the transversal force described here would exist even if the reflected wave is completely eliminated by, for example, antireflection coatings at the interface.

Another interesting observation derived from Eq.(*10*) is that the transversal force is long-range and thus can affect dipoles located far from the surface. This suggests that such lateral force should also appear for objects with dimensions larger than the wavelength.

Numerical Calculation for Larger Particles

To assess the magnitude of this transversal force for larger particles, we performed systematic numerical simulations (Comsol Multiphysics) in a geometry similar to our experiments. We evaluated the force acting on a 4.5μm polystyrene (PS) particle located at air-water interface and illuminated with circularly polarized light. Because of the large scales of this simulation ($\sim(10\lambda)^3$), special methods were developed to perform scattering calculations. The force magnitude shown in Figure 10a was calculated using a modified Maxwell stress tensor, which was integrated over a closed surface around the particle to directly take into account the asymmetry of field in the transversal direction illustrated in Figure 10b. For irradiances of 0.15mW/μm^2 , the force reaches values of tens of fN which, in principle, can be detected experimentally.

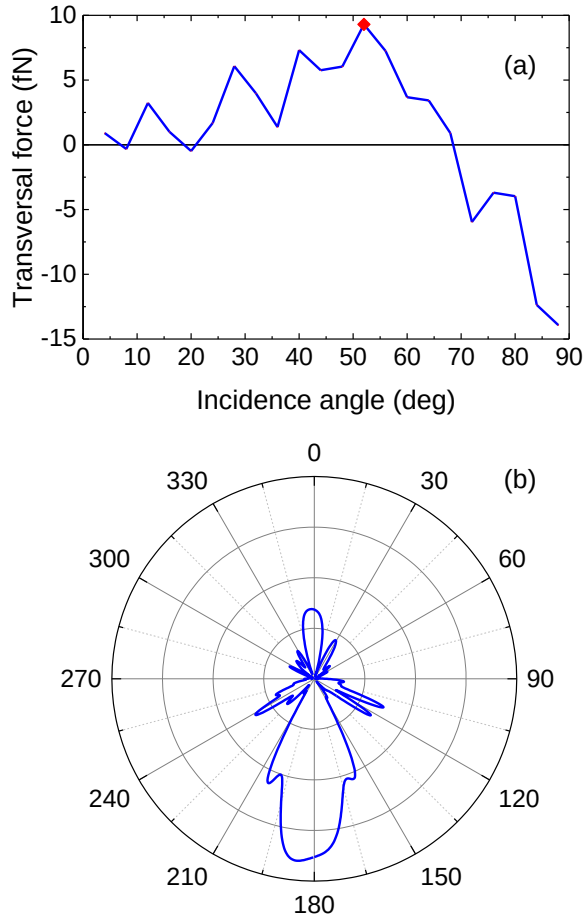

Figure 10 Lateral force on Mie-size particles. (a) Transversal force as a function of the angle of incidence for a 4.5μm PS particle located at water-air interface. The contact angle between PS and water was set to be 90 degrees [74] which makes particles to be half-submerged into water. The symbol indicates the force value at $\boldsymbol{\theta_I}$ =52° corresponding to the experimental conditions. (b) Scattering phase function in a plane transversal to the plane of incidence for incidence angle $\boldsymbol{\theta_I}$ =52°. Zero scattering angle corresponds to the direction antiparallel to the z axis in Figure 9a. The asymmetry of scattering with respect to plane of incidence is evident.

Experimental Demonstration

To verify the existence of this new type of force, we performed experiments with surface bound micro-particles. Monodispersed polystyrene (PS) microspheres with D =4.5μm diameter were deposited onto the water surface. The beam of a continuous-wave laser (wavelength 532 nm; optical power 2W) was focused into a linear trap to prevent the longitudinal movement of the particles caused by radiation pressure. In this geometry and for the highly scattering PS particles, we did not observe the interfacial tractor beam effect [66]. A rotating quarter-wave plate allowed switching between left-

and right- circular polarizations of the incident field. As can be seen in Figure 11, switching the polarizations leads to the synchronous changes in the sign of the lateral force as predicted by Eq.(9).

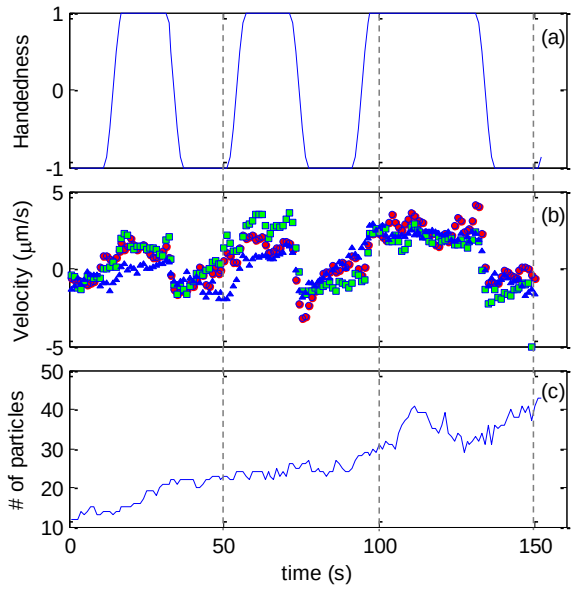

Figure 11 Experimental data. (a) Time variation of the handedness $\boldsymbol{\sigma} = \mathbf{2}\boldsymbol{Im}\left(\boldsymbol{E}_I^p \boldsymbol{E}_I^{s^*}\right)/\sqrt{\left|\boldsymbol{E}_I^p\right|^2 + \left|\boldsymbol{E}_I^s\right|^2}$ of incident wave ($\boldsymbol{E}_I^s$, $\boldsymbol{E}_I^p$ are the s- and p- components of the incident field); (b) Time dependence of lateral velocities for several particles in the linear trap. Symbols of different shape and color correspond to different particles; (c) Number of optically trapped particles as a function of time. A larger number of trapped particles results in the increased amplitude of their optically induced motion due to hydrodynamic interaction between them.

In the experiment, the weak effect of optical forces was effectively amplified by the long-range hydrodynamic interaction between particles [75, 76]. Assuming pairwise additivity, the velocity of an arbitrary particle *i* is

$$\boldsymbol{v}_i = \boldsymbol{v}_{flow} + \sum \boldsymbol{\mu}_{ij}\left(\boldsymbol{r}_i, \boldsymbol{r}_j\right)\boldsymbol{F}_\perp\left(\boldsymbol{r}_j\right) \qquad (11),$$

where $\mathbf{v}_{\text{flow}}$ is the macroscopic flow on the water surface, $\boldsymbol{\mu}_{ij}$ is the tensor defining hydrodynamic interaction [77] and the summation is performed over all particles affected by the optical force [76, 78]. The monodispersed PS particles experience the transversal force $F_\perp$ pointing in the same direction. The long-range $1/R$ hydrodynamic interactions [79] make their velocities to diverge logarithmically when increasing the number of particles. Figure 11b shows the velocities of several particles in a linear trap as a function of time. As the number of trapped particles increases over time

(Figure 11c), the particles' velocity also grows. This hydrodynamic interaction results in a three-fold increase in the observed velocities.

As evident in Figure 11b, the particles' velocity follows the changes in polarization handedness. The regression analysis performed on the base of linear model (11) yields the velocity of an isolated particle $\langle F_\perp \rangle/(3\pi\eta D/2)$ =0.62±0.06μm/s with a confidence level of 95% (the drag coefficient here is twice smaller than that of Stokes formula as particles are half in air [80]). Knowing the dynamic viscosity of water η and the size of the particles D, we evaluate the average lateral force to be $\langle F_\perp \rangle$ =11±1 fN for 0.15 mW/μm^2 average power density. This force magnitude is in excellent agreement with the predictions of numerical calculations (Figure 10a) $F_\perp^{\mathrm{theor}}(\theta_I = 52°)$ =9.3 fN.

As a side note, we do not expect SOI to produce additional spin motion of the particles. Frictional liquid forces are of the order of micro-Newtons [81], which is at least 6 orders of magnitude larger than typical optical forces.

The proposed method completes the set of methods for arbitrary manipulation of colloidal particles on the surface of liquids. Forward action is provided by the radiation pressure while backward movement can be achieved through momentum enhancement effects [66]. Here we demonstrated that a side motion can also be induced due to the transformation of spin angular momentum of incident photons into orbital angular momentum of scattered ones. To detect this new transversal force, we applied systematically, for the first time, a method of hydrodynamic amplification of opto-mechanical effects.

CHAPTER 3: CONSERVATION LAWS AT DIELECTRIC INTERFACES: EFFECT ON MATTER

An interface between two homogeneous, linear, and isotropic media introduces spatially varying optical properties (e.g. refractive index, permittivity, and permeability). During wave propagation across the interface, the change of photonic linear momentum caused by an index mismatch between media [10] can be transferred to the illuminated object resulting in a recoil force. The momentum transfer ensures the conservation of linear momentum along the interface associated with the translational symmetry. The magnitude and the direction of the optical force can be tuned by controlling the illumination conditions and the material properties and dimension of target objects and those of the surrounding medium.

Negative Optical Forces at Soft Dielectric Interfaces

In this chapter we theoretically and experimentally demonstrate electromagnetic force counterintuitively pulling arbitrary floating objects against the flow of light and along soft dielectric interfaces. The pulling action over macroscopic distances can be achieved by an appropriate modification of purely passive dielectric environment and without resorting to non-paraxial illumination, interference of multiple beams, gain or other exotic materials. The experimental data obtained by a method of video microscopy [82] were analyzed to confirm the effect.

Unlike experiments reported in Ref. [22, 83], here stable negative forces can be created even when using ordinary, unstructured, gradientless paraxial beams. The use of paraxial incident beam allows us to extend the spatial interacting regions where strictly negative nonconservative forces may occur. Hence optical manipulation based on these forces over macroscopic distances is possible.

For a physical origin of these negative forces, the forces acting against the incident beam propagation arise naturally due to the appropriate amplification of the photon linear momentum when light is scattered from one dielectric medium into another with higher refractive index. This is based

on Minkowski's formulation: the momentum of a photon increases n times upon entering the dielectric medium, $p_M = n\hbar\omega/c$, where n is the refractive index of the medium.

Numerical Calculation

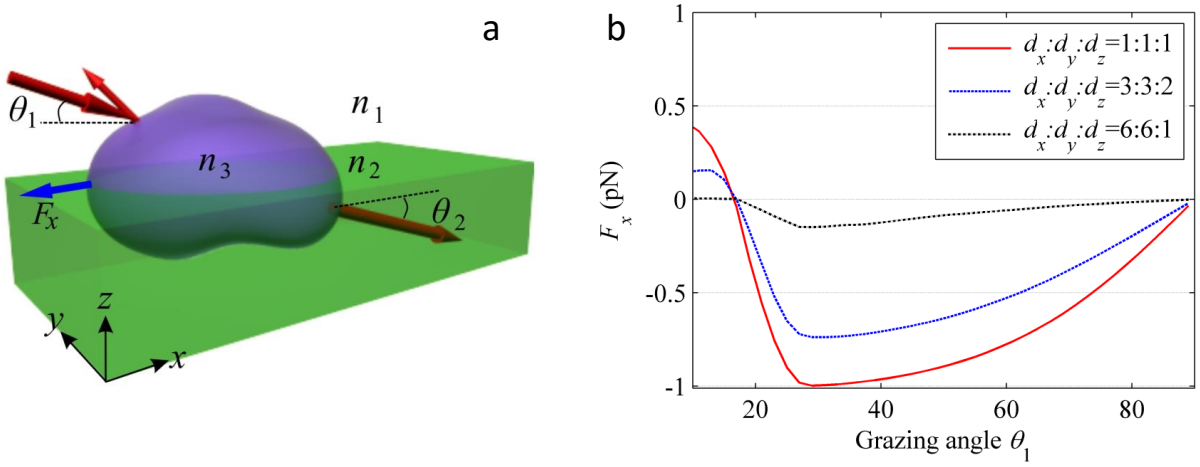

Figure 12 Forward momentum amplification and backward particle motion when a ray propagates from air into water through the scatterer. (a) Schematic illustration of the forward momentum amplification. Red arrows represent directional vectors along the incident, reflected, and transmitted rays. The lengths of the directional vectors are proportional to the refractive index of the medium that the rays lies in. As a result of momentum conservation, a negative scattering force $\boldsymbol{F_x}$ (blue arrow) is exerted on the scatterer along the interface. (b) The x-component of optical force as a function of a grazing angle $\boldsymbol{\theta_1}$exerting on spheroids with different main axes $\boldsymbol{d_x}$, $\boldsymbol{d_y}$ and $\boldsymbol{d_z}$, (see inset), while the cross-section area along interface remains the same ($\boldsymbol{d_x} \cdot \boldsymbol{d_y}$ = const, $\boldsymbol{d_x} = \boldsymbol{d_y}$ = 10μm). The forces are calculated with a ray tracing technique for spheroids with refractive index $\boldsymbol{n_3}$ = 1.42 floating at the air-water interface under the illumination of a p-polarized plane wave with the irradiance of 10 μW/μm^2.

Let us examine the situation illustrated in Figure 12**a**. A scatterer with refractive index of n_3 is placed at the interface of two media (for example, a gas and a liquid) with refractive indices n_1 and $n_2 > n_1$. The scatterer is illuminated by a beam of light (plane wave) such that some of the incident and scattered rays lie in different media, as shown in Figure 12**a**. In the conditions depicted here, both the direction and the magnitude of the momentum of the light ($\mathbf{p}_M$) change. According to Minkowski's approach, when going from medium 1 to medium 2, the momentum increases; consequently, the scattering force, in particular the component of the force experienced by the object along the interface, $F_x \propto -\Delta p_{M,x} = (\hbar\omega/c)(n_1 \cos\theta_1 - Tn_2 \cos\theta_2)$, may become negative such that the total momentum is conserved. Because the relation between θ_1 and θ_2 depends on the shape and optical properties of the system, there can be situations when the scatterer moves in a direction opposite to the incident wave. In this scheme, it is the presence of the medium with high refractive

index which provides the increase in forward momentum, even in a passive environment. Thus, according to the classification scheme discussed in ref. [26], the situation can be described as a "tractor beam" action that is assisted by the environment surrounding the object.

We note that this increase in the forward momentum depends on both reflection and refraction in the medium with higher refractive index. This is why, according to Minkowski's description, negative force would not occur, for example, for plane-parallel objects. Indeed, the angles for such an object are related according to Snell's law ($n_1 \cos\theta_1 = n_2 \cos\theta_2$) and the force along the surface is $F_x = (P/c)(n_1 \cos\theta_1 - Rn_1 \cos\theta_1 - Tn_2 \cos\theta_2) \equiv 0$, where P is the optical power incident onto the plane-parallel object characterized by the intensity reflection and transmission coefficients R and T. For objects with arbitrary shapes, a more detailed analysis is necessary to establish the detailed conditions for which negative force can be generated. As one can see from Figure 12**b**, the occurrence of negative force is a rather general phenomenon, but, of course, non-absorbing dielectric objects of different shapes could experience negative forces of different strengths. For instance, Figure 12**b** illustrates a few examples of ray-tracing calculations of scattering forces acting on objects with simple shapes (spheroids). One can clearly see that, in accordance to the discussion above, the flatter the shape of a spheroid, the smaller the negative force acting on it. Of course, at normal incidence ($\theta_1 = 90°$) there will be no component of negative force along the surface for circularly symmetric objects (Figure 12**b**).

Experimental Demonstration

To verify the concept of surface-assisted negative force, we performed a systematic experiment using small drops of dodecane (refractive index, 1.421; diameter, $\sim 10\mu m$) formed at the water surface. The small floating droplets were illuminated at a grazing angle of $25°$ by a loosely focused Gaussian laser beam (power, 1.2W; diameter, $\sim 300\mu m$). Under these conditions, the irradiance in the vicinity of the center of the illumination spot ($\sim 35 \mu W\ \mu m^{-2}$) was three orders of magnitude smaller than typical irradiances used in optical tweezers [13] and two orders of magnitude lower than in a

recent experimental realization of a tractor beam [22]. This irradiance is also small enough to leave the water surface unperturbed, in contrast to the experiments reported in Ref. [84]. The movement of microdroplets was continuously imaged with a microscope and recorded with a CCD camera. The particles' trajectories were subsequently analyzed using particle-tracking techniques.

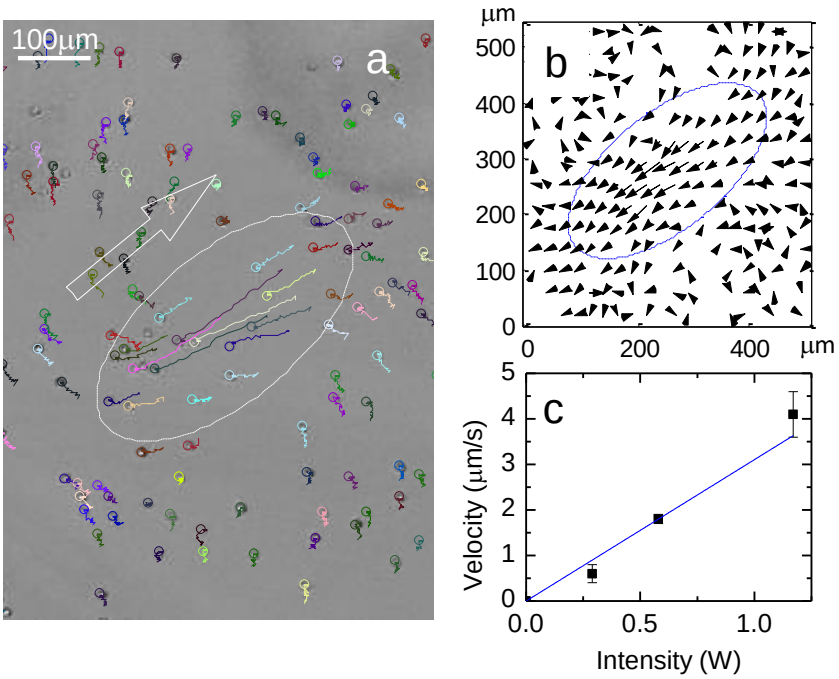

Figure 13 Pulling force action on particles bounded to water-air interface. (a) Trajectories of oil drops in the field of view of a camera during first 45 seconds of illumination with p-polarized light. The ends of trajectories are indicated by small circles and the dashed ellipse denotes the 1/e contour line of illumination spot. The arrow indicates the direction of propagation of the incident beam. (b) Average velocities (due to optical forces acting along the interface) distribution at different locations relative to the illumination spot. The length of the arrows is proportional to the average speed while their orientations indicate the local direction of movement after the contribution from macroscopic surface flows has been subtracted (see text). (c) Average velocity of oil drops near the beam's center as a function of laser input power. The error bars indicate the standard deviation of velocities distribution and the line is the linear fit to the data.

An example of reconstructed trajectories of floating particles is shown in Figure 13a. As can be clearly seen, the droplets that happen to be inside the illumination spot manifest a distinct directional motion against the beam propagation. On the other hand, particles outside the illumination spot follow different directions of motion, with trajectories influenced to a certain degree by residual macroscopic flows on the water surface and, to a minor extent, by Brownian forces. As can be seen from Figure 13**a**, negative motion of particles is observed over distances of ~200µm. In principle, the particles' movement can be affected by several mechanisms: gradient and scattering optical forces, drag forces,

and Brownian forces. At the working wavelength of 532nm, dodecane and water are essentially non-absorbing and direct thermally induced forces are not expected to make a significant contribution.

In the overdamped regime, the sum of optical and Brownian forces acting on a particle is balanced by the drag force F_d, which is proportional to the observed particle's velocity v. To remove the contribution of drag forces induced by macroscopic surface flows, we subtracted the average velocity of the particles moving outside the illumination spot from the velocities determined for particles moving inside the spot. The corrected distribution of velocities in the case of p-polarized illumination is shown in Figure 13**b** and, as can be seen, it clearly demonstrates a pronounced movement against the direction of beam propagation. Note also that, because the illumination spot is rather large, the magnitude of the optical gradient forces is insignificant. These forces do not noticeably affect the recorded trajectories, as demonstrated in Figure 13**b**, where one can see particles moving freely against the action of a potential gradient force that points from the center of the beam down and left. A distribution of velocities similar to the one in Figure 13**b** was also observed for the case of s-polarized illumination (not shown).

To study the dependence of the speed of induced movement of droplets on intensity, we performed several experiments where the illumination power was varied from 0.3W to 1.2W. The results of velocity reconstruction are shown in Figure 13**c**, where the linear dependence between these two parameters can be clearly seen.

The drag coefficient $b = F_d/v$ at the surface of the water can be assessed independently by observing the Brownian motion of the oil drops in the absence of optical excitation. In the planar geometry of interest, the mean square displacement is related to the drag constant as $\langle r^2 \rangle = 4k_B T t/b$, where k_B is the Boltzmann constant and T is the thermodynamic temperature. Using the measured drag coefficient $b = (2.3 \pm 0.1) \times 10^{-8}$ N s m^{-1} and the dependence between the observed velocity and irradiance shown in Figure 13**c**, one can establish quantitatively the relative strength of the observed component of the negative force along the interface to be $F^p/I = (2.5 \pm 0.2)$ pN/(mW μm^{-2}).

Performing a similar analysis for the s-polarized excitation, we obtain $F^s/I = (1.9\pm0.2)$ $\mathrm{pN}/(\mathrm{mW}\ \mu\mathrm{m}^{-2})$, which demonstrates the polarization dependence of the observed force.

Discussion

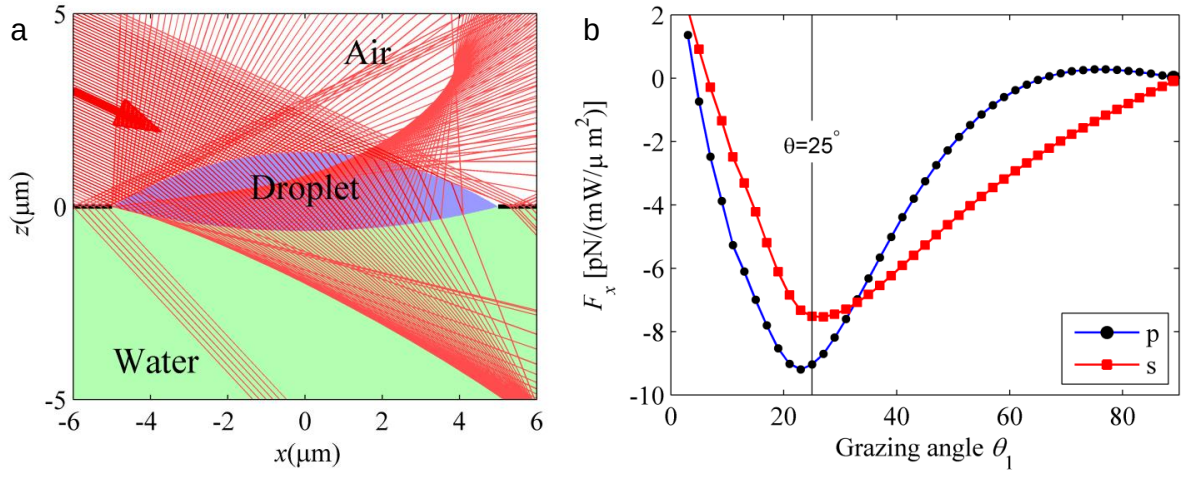

Figure 14: The optical force exerted on a lens-like oil droplet at water-air interface. (a) Example of ray tracing for a floating lenslet-shaped particle. The cross-section of the lenselet is shown and only a very low ray density is displayed for clarity. (b) The optical force acting along the interface on a lens-like oil drop 10μm in diameter as a function of grazing angle $\boldsymbol{\theta_1}$ for s- and p- polarized incident waves as indicated.

To compare the experimental results with the predictions of Minkowski's theory, one requires a correct description of the shape of the oil drops. In our experiment the oil drops were shaped as spherical lenses [85] with the surface radii defined by surface tension coefficients. Although drag and electromagnetic forces may alter the shapes of soft dielectric interfaces [10, 84], the surface tension forces in our experiment are much larger and do not allow significant deformation to the shape of the oil drops [86, 87]. Using a ray-tracing method (Figure 14**a**), we calculated the forces acting on droplets with the specific shape used in our experiments. Relating the momenta of the incident, reflected, and transmitted rays within the Minkowski formalism, we obtained the optical forces for p- and s-polarized incident waves as shown in Figure 14**b**. As can be seen from the schematic illustration in Figure 12**a**, this force is determined by the balance of three contributions to the total momentum, $\Delta\mathbf{p} = \mathbf{p}_\mathrm{I} - \mathbf{p}_\mathrm{R} - \mathbf{p}_\mathrm{T}$. The magnitudes of incident $\mathbf{p}_\mathrm{I}$ and reflected $\mathbf{p}_\mathrm{R}$ momenta in air are well defined. The apparent factor of four difference between the force measured experimentally and the value estimated numerically can be explained by a small variation of just 8% in the magnitude of the

momentum in the medium $\mathbf{p}_T$. Such deviation may be caused by several factors that were not taken into account in the model. First, the non-uniform electromagnetic field at the surface of the liquid oil drops can excite localized hydrodynamic flows that can affect the motion of the droplets. Second, the forces acting on closely spaced particles, often present in our experiment, could be different from that on a single particle, as considered in numerical estimations. Finally, there is also the possibility that interfacial phenomena (such as induced surface and interfacial charges reacting to the electric field of the incident beam [88]) in multi-phase soft matter may require refinements of the microscopic theories of optical momentum exchange and the associated mechanical action. However, all these influences are just perturbations to the major contribution to the negative force created by the amplification of the momentum in water.

In summary, we have demonstrated that gradientless optical fields can act as "tractor beams" along a properly chosen interface of two materials with different refractive indices. Based on the conservation of linear momentum, negative force can be generated without restrictions on the beam's shape, polarization, phase and so on. We note that optical forces and momentum exchange are usually discussed for objects entirely embedded in homogeneous media. The current experiment provides new insights for understanding surface effects in momentum exchange and can also assist in developing and evaluating microscopic theories of optical forces in multiphase systems and in soft bodies. This work also raises several other provocative questions. For example, could there be any specific coupling between electromagnetic and material energy-momentum tensors driven by the angular momentum conservation? This question is very interesting because light carries both angular and spin momenta, and Hall-type effects could, in principle, generate non-trivial stresses at soft interfaces showing the mechanical effect of angular momentum transfer on soft matters.

Interestingly, the effect described here does not rely on any specific coherence properties of the optical field. Indeed, it can be achieved even with incoherent light. The amplification of the forward scattering momentum is due solely to the presence of an interface between low and high refractive

index media. The phenomenology discussed here could be translated easily to other wavelength domains. In contrast to another recent “tractor beam” demonstration [22], the experiment presented here is easy scalable for arbitrarily large objects and displacements. Also, the condition for objects to have specific shapes or to be highly scattering [23] is not required. The simple scheme and the robust experimental implementation may find a plethora of applications in developing novel micromanipulation approaches and for studying interfacial phenomena.

The pushing-pulling forces as well as spin controlled lateral forces form a complete set of available methods for optical micromanipulation of matter without involving complex field structuring and control. All these electromagnetic forces are non-conservative and can act over macroscopic distances.

The role of dielectric interfaces is crucial to these peculiar optomechanical interactions. The interface breaks the centrosymmetry of the vortex field structure giving rise to the transversal force. In another situation, the amplification of photon linear momentum in the forward scattering direction occurs during the beam propagation into higher refractive index medium. The momentum transfer from light to objects generates the pulling force along the dielectric interface.

Throughout the dissertation, the conservation laws associated with the symmetry considerations prove to be a useful framework for developing unusual behavior of optical forces and thus rich light driven dynamics of matter systems.

Hydrodynamic Amplification of Optomechanical Effects

Due to a usually small magnitude of optical forces the experimental detection within high precision becomes a challenging task considering being embedded into different types of noises. The sources of these noises can be possibly from external turbulence, thermally induced fluid flow, or even thermally driven random motion of colloidal particles. One way to circumvent these is to develop highly precise particle tracking algorithm. However, its capability may be limited by several factors such as a physical appearance of an image of a particle, size of a particle in pixel, etc. An alternative way is to amplify the optomechanical effects without affecting the nature of optical forces. Here we demonstrated the hydrodynamic amplification of these effects through an efficient use of the momentum imparted to surrounding colloidal medium. In simple words, the particles moving together drag surrounding liquid creating collective and directional motion of the particles. This motion mode is called "Advection", that complements diffusion in the mass transport at low Reynolds numbers where viscous drag dominates inertia. Remarkably, we have shown both theoretically and experimentally that the enhancement effect assisted by optical advection can be achieved at low levels of optical irradiance.

In this part we demonstrate the amplification of mechanical motion induced by conventional radiation pressure exerting on colloidal particles in bulk. It should be noted that the concept was employed to enhance the experimentally detected effect of side forces briefly described in Chapter 2.

We will begin with the theoretical model that accounts for the long-range hydrodynamic interaction and then perform the experimental verification.

Theoretical background

Let us consider an unfocused beam of light propagating through a dilute colloidal suspension. Disregarding gradient forces, the optical scattering force acting on colloidal particles can be described as

$$\boldsymbol{F}(\boldsymbol{r}) = \sigma_{rp} I_{coh}(\boldsymbol{r})/c \qquad (12),$$

where σ_{rp} is the radiation pressure cross-section and I_{coh} is the *coherent* part of propagating beam. We note that only this coherent part produces an ordered movement of particles while the scattered or *incoherent* part results in randomly oriented optical forces. These random forces can lead to other interesting effects[89], but they are usually much weaker and, therefore, not relevant for the case discussed here. The decay of the coherent part of the beam in scattering medium is defined by the scattering length[90] $l_s = (n\sigma_{ext})^{-1}$, where n is the number density of particles and σ_{ext} is the associated extinction cross-section. At high intensities, a nonlinear dynamics may also develop due to an interplay between optical forces and the modified local particles concentration[1, 91]. These extreme conditions however require irradiances many orders of magnitude higher than what is considered here.

Subjected to the field of forces $\mathbf{F}(\mathbf{r})$ in Eq. (*12*), the velocity of particle *i* can be described within the additive pair-interaction approximation as a sum over stokeslets[92]

$$\boldsymbol{v}_i = \sum \overline{\overline{\boldsymbol{\mu}}}_{ij} \boldsymbol{F}_j, \tag{13}$$

where $\mathbf{F}_j \equiv \mathbf{F}(\mathbf{r}_j)$ is the force acting on particle *j*. The summation in Eq.(*13*) is performed over all the particles affected by nonzero forces. The hydrodynamic interaction between the point-like particles *i* and *j* of a dilute colloidal system is described by the Oseen tensor[92] $\overline{\overline{\boldsymbol{\mu}}}_{ij} \equiv \overline{\overline{\boldsymbol{\mu}}}(\mathbf{r}_i - \mathbf{r}_j)$

$$\overline{\overline{\boldsymbol{\mu}}}_{ii} = (6\pi\eta a)^{-1}\overline{\overline{\boldsymbol{I}}}, \;\; \overline{\overline{\boldsymbol{\mu}}}_{ij} = \left(8\pi\eta R_{ij}\right)^{-1}\left(\overline{\overline{\boldsymbol{I}}} + \hat{R}_{ij}\hat{R}_{ij}\right), \tag{14}$$

where a is the particle radius (the particles are assumed to be monodispersed), η is the dynamic viscosity of the surrounding liquid, R_{ij} is the distance between centers of the *i*-th and the *j*-th particles, $\hat{R}_{ij}$ is the unit vector in a direction from particle *j* to particle *i*, and $\overline{\overline{\mathbf{I}}}$ is a unitary matrix. One can see from Eq.(*14*) that the mobility matrix $\overline{\overline{\boldsymbol{\mu}}}$ is inversely proportional to the inter-particle distance R_{ij}. This slow dependence on R_{ij} makes the sum in Eq.(*13*) be strongly influenced by the magnitude and the spatial characteristics of the force field. In particular, it follows that by orchestrating the

particle motion with a directionally uniform field of forces, one can significantly increase particles' velocities because in Eq.(*13*) all the terms enter the sum with the same sign.

In some cases, the distance between colloidal particles is much smaller than characteristic dimensions of the beam (the width and the scattering length l_s) and the summation in Eq.(*13*) can be replaced by integration. In this case, instead of forces acting on discrete colloidal particles, one can consider volume forces acting on the fluid itself. This continuum description has been used previously in a number of situations[93-95]. When this formulation is applied to absorbing liquids in finite size vessels, the speed of optically-induced convective flows can be approximated as[93]

$$v \approx \frac{LI_0(\alpha L)}{\pi^4 c\eta} \qquad (15),$$

where I_0 is the intensity, α can be set to be equal to $1/l_s$, L is the depth of the container, c is the speed of light.

Starting from the elementary description of the velocities in Eq.(*13*), we derived an expression for the velocity of "optical streaming" in the case of deep containers ($L \gg l_s$) and wide illumination beams:

$$v \approx \frac{1}{16}\sqrt{\frac{2}{\pi}}\frac{\sigma_{rp}}{\sigma_{ext}}\frac{P_0}{c\eta w_0} \qquad (16),$$

where $P_0 = \frac{1}{2}\pi I_0 w_0^2$ is the total power carried by the beam with a waist size w_0. As one can see, the expression is qualitatively similar to Eq.(*15*), although for deep containers the velocity of optically induced flow is determined mostly by the parameters of the beam rather than the properties of the colloidal particles. An expression for the velocity of optically induced flow in a general case can be derived. One can easily estimate that, for nanometer size particles and optical beam diameters ranging from microns to millimeters, the flow velocity can be three to six orders of magnitude higher than the speed of an individual colloidal particle. The colloidal particles moving together drag the surrounding

liquid and create a significant advective flow. Manipulated particles caught in this advective flow can acquire velocities much higher than ones of hydrodynamically isolated particles.

When estimating the optical streaming velocity in Eq.(*16*), we replaced the discrete summation in Eq.(*13*) with an integration in a manner similar to the hydrodynamic description of Refs.[93-95]. However, there could be situations where the direct summation is more appropriate. This is the case, for instance, of finite-size, heterogeneous colloidal systems consisting of particles with different properties and also the case of colloids in highly focused and structured fields. These circumstances make the summation description in Eq.(*13*) ideal for describing micro-fluidic applications. It could be noted that the discrete-colloid approach used in Eq.(*13*) can be seen as an analog of the discrete dipole approximation (DDA) in electrodynamics [96] and, correspondingly, the area of application of discrete-colloid approach can be similar to the one of DDA.

Experimental Demonstration

To verify the proposed concept of the hydrodynamic amplification, we performed systematic experiments with microscopic 4.5μm-diameter polystyrene (PS) particles. First, we investigated a particle motion in the absence of optical advection. PS particles were dispersed onto the surface of water over an area of ten millimeters in diameter. The method for depositing microspheres on the liquid surface was described in Ref.[97]. The motion of the particles at the air-water interface was imaged through a $\times 10$ microscope objective (NA 0.25, Olympus) and recorded by a CCD camera (Andor sCMOS) with a frame rate of 25 f.p.s. The motion of PS particles was recorded and particle-tracking techniques were applied to analyze the particles' trajectories. In the absence of the light illumination, the PS particles experience a Brownian motion. The diffusion coefficient can be experimentally measured from the relative mean square displacements $\mathrm{MSD_{rel}}= \langle \Delta r_{rel}^2(\tau) \rangle$ [98]. Figure 15 shows the relative mean square displacements of PS particles as a function of time lag τ. The corresponding diffusion coefficient is $0.0836 \pm 0.0002 \mu m^2/s$, which corresponds to an average displacement of 2.68μm over 10s duration. Experimentally found diffusion coefficients are

approximately two times lower than the theoretically estimated value (~0.22μm^2/s). The theoretical value of diffusion coefficient for surface bound particles is found by knowing the contact angle (that is $\approx 90°$ for PS and water [99]) and corresponding submergence depth for polystyrene [87]. In particular, PS particles are half-submerged into water that makes their diffusion coefficient twice larger than that for the particles in a bulk. The reduction of the diffusion coefficients of the particles can be due to surface contamination.

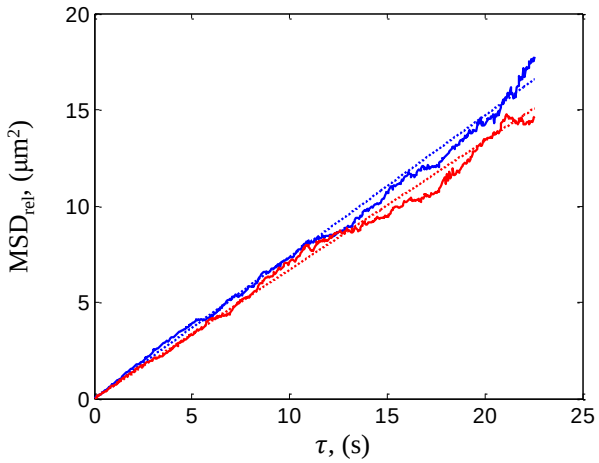

Figure 15 The temporal evolution of the relative mean square displacements of diffusing targeted particles. Particles are placed on the surface of pure water (red color) and on the surface of a colloidal suspension of polystyrene nano-particles (blue color).

After measuring the diffusion coefficient, the system was illuminated by a linearly polarized monochromatic unfocused light from a CW laser (Coherent Genesis CX Series model; wavelength 532 nm; optical power 2.5W; beam diameter 2.2mm) at the incident angle of 27°. Two 532 nm notch filters (OD4, from Edmund) were used to remove the scattered laser light. At the operating wavelength of 532nm, the absorption in polystyrene and water is minimal and causes only negligible thermal contributions meaning that all the mechanical effects of light can be attributed to the exchange of linear momentum. We found that the micro-particles placed on the surface of pure water are pushed along the beam propagation with a maximum velocity $v \approx 0.72$ μm/s. The distribution of velocities is depicted in Figure 16 with blue color.

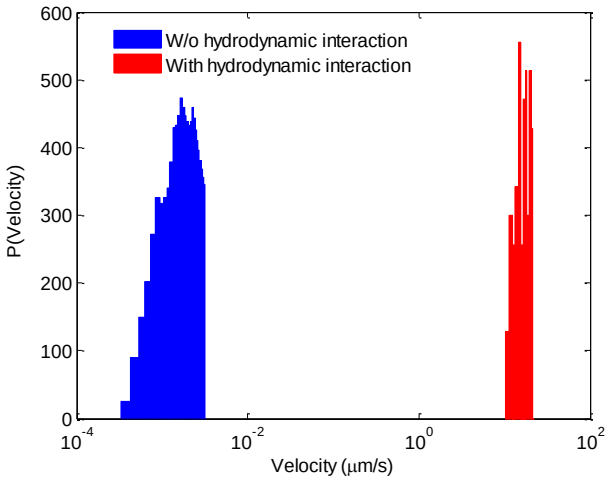

Figure 16 Probability density functions of velocities for 4.5μm PS particles propelled by laser irradiation. PS particles are uniformly distributed on the surface of pure water (Blue color) and on the surface of a monodisperse colloidal suspension of polystyrene nano-spheres (Red color) under the laser illumination with optical powers of 2.5 and 0.3 W, respectively

Next, we estimated the effectiveness of the hydrodynamic amplification. Polystyrene microspheres were placed onto the surface of colloidal suspensions containing 0.3%v/v colloidal concentration of 200-nm-diameter polystyrene particles. The measured diffusion coefficient in the absence of external illumination was 0.0919±0.0002μm^2/s (see Figure 15), which is close to the case of PS particles placed on the surface of pure water. Following the measurement of diffusion coefficient, the colloidal system was illuminated by a CW laser beam with 0.3W optical power and with all other parameters being the same as in the previous case. After switching on the illumination, the particles on a surface started immediate motion and continued to move until light was turned off. An example of reconstructed trajectories of floating particles is shown in Figure 17a. The center of the illuminating beam lies in the middle of the image and, as can be clearly seen, the particles in that vicinity experience a directional motion along the beam propagation. The spatial distribution of velocities of interfacial particles is shown in Figure 17b while the corresponding histogram of the velocity magnitudes is displayed in Figure 16 (red color). The maximum velocity of the particles observed in experiment is 22.3 μm/s. It can be clearly seen that, in this case, the velocities are one order of magnitude larger than the velocities measured on the surface of pure water. It also should be reminded that these values were obtained for an optical power of illumination $P_0 = 0.3$W, which is almost one order of magnitude lower than the power used in the case of pure water. With a diameter of incident

beam being 2.2mm, the irradiation intensity in our experiment was $0.16\mu W/\mu m^2$ that is 2 orders of magnitude less than in the experiments with evanescent waves [100-102]. With this low intensity level we could achieve several times higher propulsion velocities because of an efficient 'recycling' of the lost energy through the colloidal particles.

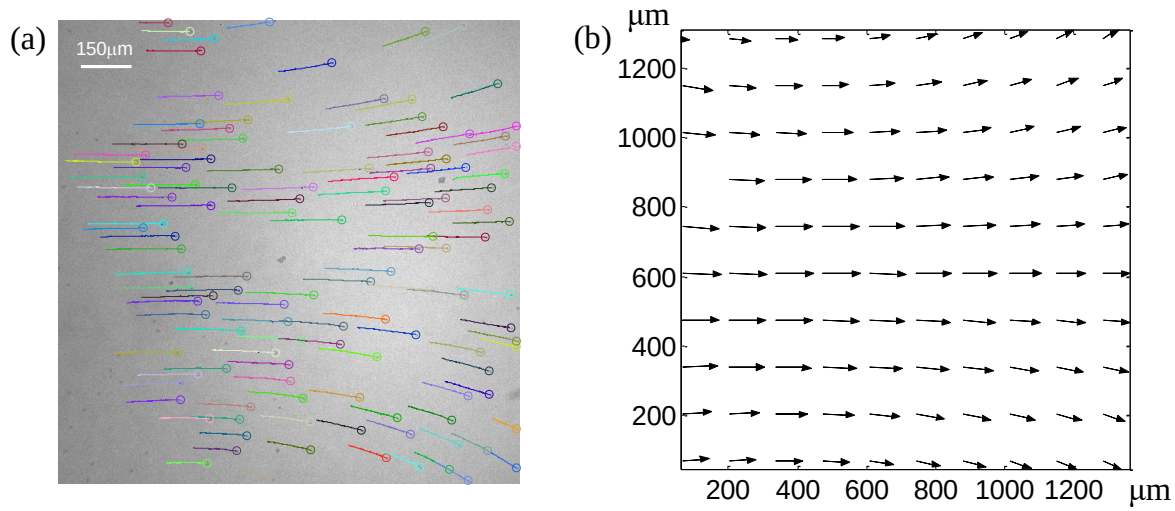

Figure 17 Hydrodynamic amplification experimentally observed at the surface of the colloidal suspension. (a) Trajectories of interfacial particles during the 10s of laser illumination. The ends of trajectories are indicated by small circles. (b) Spatial distribution of time-averaged velocities. The length of the arrows is proportional to the speed while their orientations indicate the local direction of particles' motion.

Additional results illustrating the hydrodynamic amplification in a different type of colloid are presented (not shown here). That experiment made with silica colloidal particles also shows the significant increase of velocities of their mechanical motions.

In principle, the achievable advective velocities can be even higher. To prove that, we performed extended numerical calculations of advective flows with the same parameters as in experiment while considering the situation of negligible contributions from the container walls. Calculations show that the velocity of advective flows can achieve a maximum speed of $\approx 190\,\mu m/s$. The measured velocities in the experiment are an order of magnitude lower, which could be explained by the finite dimensions of the cuvette; it is known that backflow of displaced water outside the region of action of optical forces apparently slows down the induced advection [95]. In addition, the reduced measured velocities

of the particles could be a consequence of possible surface contamination that also explains lower measured diffusion coefficients of PS particles.

We should point out that the hydrodynamic interaction between large numbers of particles can be harnessed to not only amplify the optomechanical effects to be experimentally detectable but also achieve optically controlled transport. In this case the mass transport assisted by optical advection can be tunable by the characteristics of light and illumination condition. We note that the proposed concept of controlled transport can be generalized and implemented with different external driving forces. For instance, fluid flows can be generated by applying time-dependent biaxial magnetic fields to magnetic platelet suspensions [103, 104]. Complex flow patterns can be externally controlled by the specific properties of both the applied fields and suspended particles, enabling tunable heat and mass transport [104]. However, the magnetic forces are usually much stronger than the optical ones leading to higher velocities of turbulent flows at high Reynolds numbers that may alter the transport.

Conclusions

In conclusion, we proposed and demonstrated ability of amplification of optomechanical effects through advection mechanism that can be controlled optically. The proposed concept can be applied to optical manipulation inside a volume and at the interface.

The experimental results presented here show the hydrodynamic amplification of conventional radiation pressure exerted on the colloidal suspension of 200 nm diameter PS particles. The collective effects were observed from the motion of 4.5 μm diameter tracer particles along the surface of the colloidal suspension because of much simpler detection system. In this situation the radiation pressure cross-section of the 200 nm-diameter PS particle is extremely small, resulting in a particle velocity of several nm/s for a Watt-level illumination. In addition, the diffusion of the nanometer size particle dominates its directional motion, making it even harder to be detected. Also, because of diffraction limit, the light cannot be deployed only over the targeted area of a particle and a large part of radiation is practically lost. The proposed concept of the hydrodynamic amplification allows us to ‘recycle’ the

lost energy and to use it efficiently for manipulating the particles. As such, the velocity of 200nm particles caught in the advective flow would reach hundreds μm/s even when the irradiation power is one order of magnitude smaller (~100mW).

Besides, the hydrodynamic technique permits to effectively regulate the mass transport in a remote, noninvasive, and, most importantly, in a power efficient manner, which should be of interest for microfluidic lab-on-chip platforms.

At this stage we form for the first time a complete set of nonconservative forces for arbitrary manipulation of objects at liquid surface with unstructured light beam at low irradiance. We gain a complete control over the magnitude and direction of mechanical motion of microscopic objects relying on different electromagnetic interactions, governed by conservation laws as well as the long-range hydrodynamic interaction. These are consequences of electromagnetic interactions on matter.

In the next chapter we will shift our focus to the effects of optical manifestations on electromagnetic waves.

CHAPTER 4: CONSERVATION LAWS AT DIELECTRIC INTERFACES: EFFECT ON LIGHT

Beam Shifts

Fundamentally, light experiences reflection and refraction upon interacting with the refractive index gradient. The optical interaction of a plane wave with a plane dielectric interface between two non-magnetic, isotropic, and homogeneous media is described by well-known Snell's law and Fresnel formulae which relate propagating vectors and field amplitudes of incident and secondary waves, respectively [105]. This provides simple geometrical optic description of light evolution. However, the situation becomes more complicated for a real optical beam with finite width (i.e. angular spectrum). The reflected and transmitted beams are subject to subwavelength beam shifts, deviating from the geometrical optic prediction.

There are basically four types of beam shifts measured with respect to the plane of incidence, in-plane spatial and angular shifts (called Goos-Hanchen shift [106]) and out-of-plane spatial and angular shifts (called Imbert-Fedorov shift [107]). The schematic picture of these beam shifts can be found in Ref.[36]. Their origins can be well understood within self-consistent framework centered on beam transformations and deformations at the interface [36]. The GH shifts are associated with the in-plane angular dispersion of reflection and transmission coefficients while the transverse IF shifts relate to the geometric phase distributed across the angular spectrum.

It is important to note that the spatial IF beam shift is a consequence of conservation of angular momentum. Because of the rotational symmetry of the material system about a z-axis (normal to the interface), the z-component of the total angular momentum (SAM and intrinsic and extrinsic OAM) must be conserved upon reflection and transmission. As a result of light-matter interaction at the interface, the net change of the z-component of the SAM is converted into the extrinsic OAM along the z direction. The spin-orbit transfer gives rise to the transverse shift of the centroid of the optical

finite beam along the y direction. It is noted that the incident beam is assumed to not possess the intrinsic OAM.

As an optical analog of electronic spin Hall effect, upon interacting with a refractive index gradient a linearly polarized wave splits into left and right circularly polarized waves experiencing opposite signs of spin dependent transverse spatial shifts at the interface [38, 108-110]. This transversal spin transport is widely known as “spin Hall effect of light (SHEL)” that resembles the IF beam shift.

In principle, the spin-orbit coupling should assist in processing and communicating information encoded as spin and orbital angular momentum states of a light beam. However, due to small magnitude of photon momentum the weak SOI requires sophisticated detection scheme for measuring SHEL [38]. The ability to enhance SHEL in a controllable manner is desired. Recently, it was demonstrated that the rapidly varying phase gradient along a metasurface introduces strong SOI resulting in a large splitting of polarized light [111]. The position-dependent phase retardation can be tailored by adjusting the length and orientation of the arms of the V-shaped gold antennas patterned on the surface, allowing us to tune the SHEL. Conceptually, the spatially varying phase distribution imposes additional momentum on an incident wave leading to the large SHEL. Nevertheless, the use of lossy material and complexity of fabrication process make metallic metasurface less practical platform for spin-controlled photonics. Recently, we theoretically proposed to anomalously enhance the SHEL by obtaining large phase retardation attributed to an effective anisotropy of a metal-dielectric composite. The effective optical anisotropy is induced due to the presence of an inevitable surface that breaks the translational symmetry of electromagnetic field in the direction perpendicular to the surface. The existence of induced effective anisotropy seems counterintuitive considering that the composite consists of components that are isotropic in shape, distribution, and optical properties. Before investigating the anomalous SHEL at a composite interface, let us qualitatively and quantitatively describe several proposed mechanisms contributing to “surface induced anisotropy” (SIA). This should provide us physical insight of an origin of the anomalous SHEL.

Beam Shifts at Composite Interface

Surface Induced Anisotropy of Composite Material

Optical anisotropy can be either an intrinsic material property or an effective response due to complex structures. The effective anisotropic properties can still exist even in optical media with highly symmetry of distribution, shape, and optical properties. We show that inhomogeneous media consisting of spherical constituents randomly and uniformly distributed inside a host medium with isotropic optical constants can exhibit effective anisotropy due to the inherent presence of the surface [112]. As will be seen, such composite media possess different effective refractive indices for *s*- and *p*-polarized incident light.

In the following, different mechanisms that can lead to SIA will be discussed.

Mechanisms for surface-induced anisotropy

One can single out several mechanisms that can contribute to surface induced anisotropy in randomly inhomogeneous media having macroscopically isotropic properties.

The first mechanism relates to the fact that inclusions cannot penetrate the surface. As a result, the concentration of inclusions in the vicinity of the surface will be smaller than that in the bulk as illustrated in Figure 18. According to effective medium theories, a change in the concentration of inclusions leads to a change in the effective refractive index. Thus, a thin layer situated near the interfaces of an inhomogeneous slab will have slightly different refractive indices. It is known that such multilayer structure will manifest anisotropic effective properties [113-115]. However, because the thickness of the regions having different refractive indices is of the order of the size of inclusions, only small changes are induced in the magnitude of the refractive index of the slab and one cannot expect sensible effects due to this mechanism.

We note that the surface penetrating inclusions can be sectioned along that surface and, in this case, the concentration of inclusions can be constant across the entire volume. However, the truncated

inclusions will now lose their spherical symmetry and their anisotropic shape will again induce surface anisotropy.

Another mechanism that could lead to surface-induced anisotropy relates to the change in local fields near the surface [116, 117]. The local field at the position of some inclusion is determined by surrounding inclusions located within the so-called Lorentz sphere drawn around the observation point as shown in Figure 18**b** [116]. When the observation point is close to an interface, the Lorentz sphere is truncated and the distribution of local fields inside the sphere changes. The magnitude of local field inside the truncated sphere will depend on polarization of incident wave and this determines the anisotropic behavior of the surface layer. Also, this means that the effective refractive indices for thin slabs of inhomogeneous materials will be different for *s*- and *p*-polarized incident wave. We should mention that the anisotropy of dielectric permittivity caused by finite size of particles and retardation effects (Drude transition layer) was discussed previously in the case of plasmonic metamaterials with periodically arranged metallic inclusions [118-120]. The authors of these papers note that the presence of surface does require a more careful description of the metamaterial slab's optical properties.

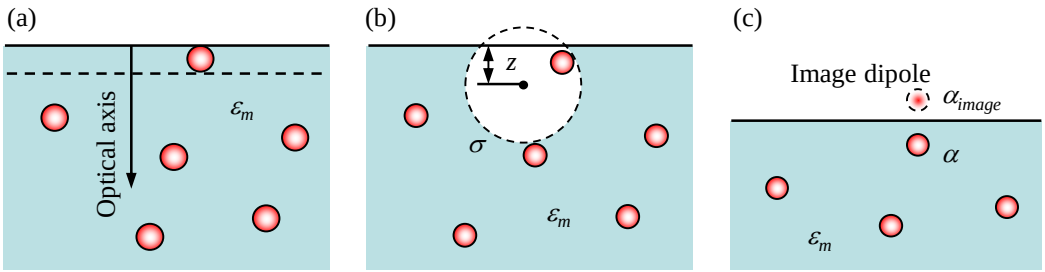

Figure 18 Surface induced anisotropy can be attributed to (a) change in the concentration of inclusions, (b) modification of local field, (c) inclusion-surface interaction.

A third mechanism for the surface-induced anisotropy can be simply explained by the interaction between the inclusions and their own images with respect to the surface as illustrated in Figure 18**c**. This interaction changes the polarizability of inclusions located near the surface and, consequently,

modifies the effective properties of the medium near the surface. We expect this effect to be significant for metallic inclusions.

Local field changes near the surface

A simple analytical theory for surface layers of inhomogeneous media that takes into account local field change near the surface is described in [121] where the effective permittivity of a medium containing small spherical inclusions arranged in a cubic lattice was considered. In the electrostatic approximation, it was demonstrated that dielectric permittivity at different depths *z* is [121]

$$\varepsilon_t(z) = \varepsilon_0 + \frac{N\alpha}{1-N\alpha C_t(z)/\varepsilon_0},\ \varepsilon_n(z) = \varepsilon_0 + \frac{N\alpha}{1-N\alpha C_n(z)/\varepsilon_0}, \quad (17),$$

where ε_t and ε_n are the dielectric permittivities along the directions tangential and normal to the surface, N is the number density of inclusions, and α is the polarizability. The depth-dependent coefficients are $C_t(z) = 0.346$ and $C_n(z) = 0.307$ in the layer closest to the surface; in the bulk these coefficients become $C_t(z) = C_n(z) = 1/3$. Material parameters averaged across the layer of thickness h can be found according to the following rules [122-124]

$$\varepsilon_h^t = \frac{1}{h}\int_0^h \varepsilon_t(z)dz\ ,\ \varepsilon_h^n = h\left(\int_0^h \frac{dz}{\varepsilon_n(z)}\right)^{-1} \quad (18).$$

Several conclusions can be reached in this electrostatic approximation. First, according to Eqs. (17) and (18), thin inhomogeneous slabs behave as uniaxial anisotropic materials with the optical axis directed perpendicularly to the surface. Ordinary and extraordinary refractive indices of these slabs can be found as $n_o = \sqrt{\varepsilon_h^t}, n_e = \sqrt{\varepsilon_h^n}$. Second, the refractive index for s-polarized waves (the same as the ordinary refractive index n_o) does not depend on the angle of incidence. The refractive index for p-polarized waves n_p on the other hand is a function of angle of incidence as shown in Figure 19. Note also that, according to Eq. (18), the degree of anisotropy increases when the thickness of the slab decreases.

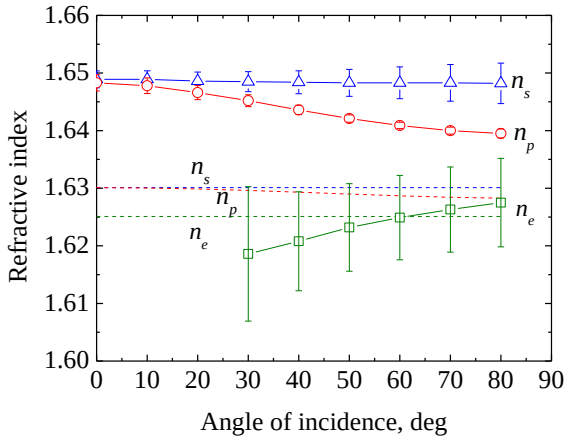

Figure 19 Effective refractive indices $\boldsymbol{n_s}$, $\boldsymbol{n_p}$ and $\boldsymbol{n_e}$ as functions of the angle of incidence as calculated with Eq. (***18***) (dashed lines) and calculated by electrodynamic simulations (solid lines) for a 135 nm thick inhomogeneous slab having 25% volume fraction of inclusions with radius $\boldsymbol{r} = 25$ nm and refractive index $\boldsymbol{n_i} = 2.97$ embedded into a matrix of refractive index $\boldsymbol{n_m} = 1.33$. The error bars indicate the uncertainty in reconstructing the average values of refractive index with confidence 0.95.

The simple analytical theory leading to the depth-resolved dielectric permittivity expressed in Eq. (17) allows one to describe the optical properties of thin layers with inclusions much smaller than wavelength, which are assumed to be arranged in a regular lattice inside the host matrix. To describe the optical properties of layers with random structure, we should approach the problem differently. Also, in a situation where the distances between individual inclusions lay in the range of hundreds nanometers, the retardation effects will start manifesting in the interaction between different inclusions. To fully explore the surface effects in this case, one should go beyond the electrostatic approach and perform numerical electrodynamic calculations.

There are different methods to calculate the transmission of optical wave through inhomogeneous slab such as, for example, Finite-Difference Time Domain, Finite Elements Methods (FEM), Coupled Dipole Method based on periodic boundary conditions [125], three-dimensional layered KKR method [126]. In this work we used Finite Elements Method implemented in commercial software Comsol Multiphysics 3.5a. This approach offers a convenient way to describe the properties of systems containing both dielectric and metallic inclusions. Periodic boundary conditions were applied to the volume containing small spherical inclusions. This allows us to replicate this volume in two dimensions and produce a pseudo random slab structure.

In our numerical experiment, randomly inhomogeneous slabs were illuminated by *s*- and *p*-polarized plane waves and the complex reflection and transmission coefficients were derived from the fields on the entrance and exit surfaces of the slab. The procedure was repeated for different spatial distributions of inclusions in order to determine average values for the reflection $r_{s,p}$ and transmission $t_{s,p}$ coefficients. Subsequently, these complex valued amplitudes $r_{s,p}$ and $t_{s,p}$ corresponding to the *s*- and *p*-polarized incident wave were used to infer the values for refractive indices attributed to the inhomogeneous slabs. Standard recovery procedures are described in [127] for the case of a plane wave normally incident on the slab. For arbitrary angles of incidence, the relation between refractive index and the amplitude reflection and transmission coefficients is found to be [128]

$$cos\left(k_0 h\sqrt{n_{s,p}^2 - sin^2\theta}\right) = \frac{1-r_{s,p}^2+t_{s,p}^2}{2t_{s,p}} \quad , \tag{19}$$

where θ is the angle of incidence. If we regard the simulated inhomogeneous layer as a material possessing uniaxial anisotropy and having the optical axis perpendicular to the surface (see also Figure 18), then the ordinary refractive index will coincide with n_s while the extraordinary refractive index will be given by

$$n_e = \frac{n_o \, sin\,\theta}{\sqrt{n_o^2 - n_p^2 + sin^2\theta}} \tag{20}$$

First, we performed calculations on a slab of thickness 0.253λ ($\lambda = 532$ nm) containing inclusions with refractive index $n_i = 2.97$ embedded in a matrix with refractive index $n_m = 1.33$. The radius of inclusions $r = 25$ nm is much smaller than the wavelength of radiation. The volume fraction of inclusions is $f = 0.25$ corresponding to an average inclusion-inclusion separation equal to 64nm, which is again much smaller than the wavelength. The values of these parameters ensure that an electrostatic description is appropriate. The recovered values of the refractive indices are illustrated in Figure 19 for slabs illuminated at different angles of incidence θ. Transcendental Eq.(*19*) allows multiple solutions for refractive indices $n_{s,p}$. We chose the correct solution as the one closest to the

effective index predicted by Bruggeman effective medium theory. We used Bruggeman's theory because it allows rather large volume fractions of inclusions in comparison with Maxwell-Garnett model. For each angle of incidence we used 400 different realizations of the inhomogeneous slab. The error bars in Figure 19 indicate the uncertainty in reconstructing the average values of refractive index with confidence 0.95. We note that at small incidence angles the difference $n_o^2 - n_p^2$ in the denominator of Eq.(*20*) introduces large uncertainties in the reconstruction of the extraordinary refractive index n_e, thus n_e is not shown for small angles of incidence.

As can be seen in, the overall behavior of the refractive indices is similar to the electrostatic predictions. Namely, within the uncertainties in reconstruction, both the ordinary and extraordinary indices are rather independent of the angle of incidence. Nevertheless, numerical calculations predict much larger differences between ordinary and extraordinary refractive indices than electrostatic theory.

The qualitative agreement between the predictions of an electrostatic theory and the results of our electrodynamic calculations shown in Figure 19 demonstrates the validity of modeling and refractive index reconstruction procedure. Therefore, we can now examine the situation of an inhomogeneous medium with parameters far from the electrostatic limit. In our next example we considered a composite slab with the same dielectric parameters as in the previous case and having the same concentration of inclusions but with twice larger thickness 0.506λ and twice larger size of inclusions $r = 50$ nm. The electrostatic theory for this case would produce the same results as depicted in Figure 19. The refractive indices in electrodynamic calculations for the s- and p-polarized incident waves were reconstructed for different angles of incidence. Around 100 realizations of inhomogeneous sample were used for each angle of incidence. The results of reconstruction procedure are shown in Figure 20. As one can see, the behavior of the refractive indices in Figure 20 is quite different from that seen in the electrostatic case and in the case of small inclusions and thin slabs presented in Figure 19. In particular, we note that the refractive indices exhibit anomalous behavior in vicinity of 30° and

60° angles. This anomalous, resonance-like behavior at specific angles of incidence is also observed for the reflection and transmission coefficients and it corresponds to the special cases when the optical paths inside the slab equal to 1.5λ and 2λ for incidences at 30° and 60°, respectively. The fact that this anomalous behavior occurs at different angles for n_s and n_p clearly shows that these refractive indices are different. On the other hand, this anomalous behavior of the effective refractive indices indicates that the inhomogeneous slab acts as an effective multilayer structure, which cannot be described satisfactorily by a single effective (anisotropic) index. As the anomalous behavior in Figure 20 is determined by surface layer, the observation of such a behavior of reflectivity in experiment can be used for estimating the properties of this surface layer (refractive index, thickness, and, as a consequence, the particle-particle separation).

We note that if one attempts to calculate the extraordinary refractive index n_e according to Eq.(*20*), the results are quite irregular indicating that such inhomogeneous slab does not behave as a simple uniaxial crystal.

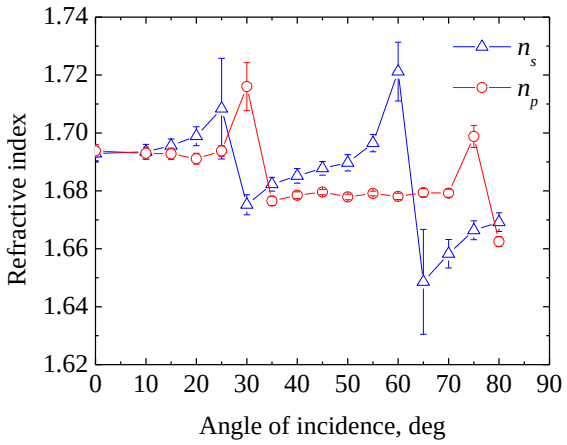

Figure 20 Reconstructed refractive indices based on reflection measurements at different angles of incidence. Vertical bars denote the uncertainty in reconstructing the average values of refractive indices for inhomogeneous slabs characterized by inclusions with refractive index 2.97, radius 50nm, and volume fraction 25% in the host medium with refractive index 1.33. Slab thickness is 269nm.

In the examples above we considered the situations of dielectric composites for which the main mechanism contributing to the perceived anisotropy of the refractive index is the one depicted in

Figure 18**b**. However, in many other applications, metal-dielectric composites are of interest. For these types of composites other mechanisms leading to surface anisotropy can also play role. As schematically illustrated in Figure 18**c**, the surface-inclusion interactions can further increase surface induced anisotropy. These mechanisms will be discussed in the next section.

Surface anisotropy induced by image dipoles

Modifications of effective refractive indices due to interaction with image dipoles can also be described based on a generalized Maxwell-Garnett theory. As shown in Figure 18**c**, a spherical inclusion placed near a planar interface induces an image dipole

$$\boldsymbol{d}_{im} = \frac{\varepsilon_m - 1}{\varepsilon_m + 1}\left(d_x, d_y, -d_z\right) \qquad (21).$$

Because of interaction with its image, the effective polarizability of such inclusion becomes anisotropic and also dependent on the distance of inclusion to the surface *z*

$$\overleftrightarrow{\boldsymbol{\alpha}}_b^{eff} = \begin{pmatrix} \alpha_t & 0 & 0 \\ 0 & \alpha_t & 0 \\ 0 & 0 & \alpha_n \end{pmatrix}$$

$$\alpha_t = \alpha_b\left(1 + \frac{1}{\varepsilon_m}\frac{\varepsilon_m - 1}{\varepsilon_m + 1}\frac{\alpha_b}{8z^3}\right)^{-1}, \quad \alpha_n = \alpha_b\left(1 + \frac{1}{\varepsilon_m}\frac{\varepsilon_m - 1}{\varepsilon_m + 1}\frac{\alpha_b}{4z^3}\right)^{-1} \qquad (22).$$

The effective polarizability of this inclusion can be related to the effective permittivity $\overleftrightarrow{\boldsymbol{\varepsilon}}_{eff}$ of the composite in the surroundings of this inclusion using Maxwell-Garnett approach:

$$\frac{4\pi}{3} N \overleftrightarrow{\boldsymbol{\alpha}}_b^{eff} = \frac{\overleftrightarrow{\boldsymbol{\varepsilon}}_{eff} - \varepsilon_m}{\overleftrightarrow{\boldsymbol{\varepsilon}}_{eff} + 2\varepsilon_m} \qquad (23).$$

where *N* is number density of inclusions. Using Eq. (*23*) in Eq. (*18*), one can determine an average permittivity of the randomly inhomogeneous layer.

For dielectric inclusions, the corrections to the refractive index become negligibly small. Indeed, because the inclusions cannot be situated at distances closer than their radius a and the effective polarizability of inclusions is

$$\alpha_b = a^3 \frac{\varepsilon_b - \varepsilon_m}{\varepsilon_b + 2\varepsilon_m} \tag{24}.$$

The denominators in the expressions of Eq. (*22*) behave as $1 + \xi$ with $\xi \ll 1$ for dielectric inclusions situated near the surface. For deeper inclusions, their contributions decrease even further as $(a/z)^3$.

However, in the case of metallic inclusions, a much different situation develops. If $\mathrm{Re}(\varepsilon_b) = -\varepsilon_m$ and $\mathrm{Im}(\varepsilon_b) \ll 1$, which can be encountered for metals, according to Eq. (*22*) the magnitude of the polarizability will be quite large. Similarly, for certain concentrations of inclusions and certain depth positions, the denominators in Eq. (*22*) can become very small locally therefore increasing the effective permittivity. It is also important to emphasize that, as can be seen from Eq. (*22*), the resonant conditions are not the same for all the components of the polarizability tensor. This may lead to significant differences between the effective ordinary and extraordinary refractive indices.

To evaluate the behavior of dielectric parameters in the presence of metallic inclusions, we performed a full electrodynamic computation of both transmission and reflection from randomly inhomogeneous slabs containing subwavelength size metallic inclusions followed by an effective index reconstruction similar to that formulated in preceding section. In this case, the change of spatial distribution of metallic inclusions and other structural parameters can result in relatively large variations of reflection and transmission coefficients, so an average of approximately 200 realizations for each concentration of metallic inclusions was taken in order to represent the effective properties of the random structure. Retrieving the effective optical properties required solving the transcendental Eq. (19), which inevitably involved making a choice from several possible solutions. To appropriately describe the physical situation in the numerical experiments, this selection process should be independent of any effective medium theory. Among various methods [127, 128], generalized bounds

for the complex effective permittivity can be graphically formed in complex plane to choose the correct roots at low volume fractions but still allow the possibility of potentially multiple solutions at higher concentration values [129]. In our case, we selected the appropriate solutions by ensuring the continuity of the retrieved indices starting from the case of the host medium without any inclusions (zero volume fraction of metallic inclusions).

In the numerical calculations we investigated a slab of thickness 0.506λ ($\lambda = 532$ nm) containing 50nm-radius Ag inclusions with refractive index 0.129+3.193i [130] which were randomly distributed into a host medium with refractive index 2 and illuminated at a fixed angle of incidence 60°. Estimations based on the electrostatic theory using Eqs.(17),(*18*), and (*23*) indicate that the local field modification near the surface and the interaction with the image dipole both result in a similar degree of anisotropy of inhomogeneous slab.

In the numerical calculations, for each of concentration of metallic inclusions, the reflection and transmission coefficients were numerically computed and subsequently the reconstructed refractive indices were obtained using Eqs.(*19*) and (*20*). The real and imaginary parts of the effective s-, p-, ordinary, and extraordinary refractive indices are shown in Figure 21.

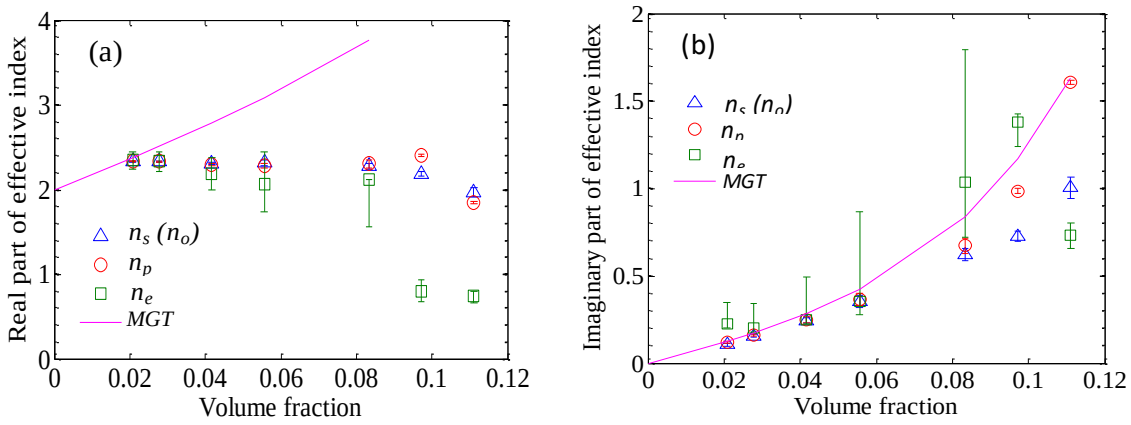

Figure 21 The real (a) and the imaginary (b) parts of reconstructed effective refractive indices as a function of volume fraction of 50 nm-radius Ag inclusions with refractive index 0.129+3.193i embedded in a host medium with index 2. The reflection and transmission coefficients were measured from a slab of thickness 0.506λ (λ=532 nm) illuminated at 60° incidence. The error bars indicate the uncertainty of average values of refractive indices with a confidence level 0.95. The solid line represents the effective indices estimated based on Maxwell Garnett theory (MGT).

A number of observations can be summarized based on the results in Figure 4. As can be seen, the degree of optical anisotropy can be relatively large even for low concentration of inclusion at the level of 10% volume fraction. In addition, the real part of the numerically reconstructed refractive indices deviates quite significantly from the estimations of the effective medium theory while the imaginary part is in rather good agreement with the Maxwell-Garnett results. It is clear that Maxwell-Garnett effective medium theory can't describe well the complex behavior of these reconstructed refractive indices qualitatively. This happens because the electrodynamic approach accounts directly for near-field interactions between different inclusions, multiple scattering, and nonuniformity of field inside inclusions, in contrast to the Maxwell-Garnett model based on an electrostatics description. Moreover, it is quite inappropriate to assign one isotropic effective refractive index to inhomogeneous medium with nonuniform 3D spatial distribution of inclusions. The trend of imaginary part of reconstructed indices can be explained by the simple fact that a higher fraction of metallic inclusions increases the absorption at the off-resonance conditions. Such increase of absorption should be expected even in the simple electrostatic model.

The presence of an air-composite interface breaks a translational symmetry of electromagnetic field along a direction normal to the surface. The loss of field symmetry and the inclusion-surface interaction lead to an anisotropic modification of effective permittivities of surface layer. This should offer another route to engineer spatial gradients of anisotropic properties in metamaterials operating in the optical regime.

In the next section we will discuss the role of surface induced anisotropy on the spin transport.

Anomalous Phase Retardation and Spin Hall Effect of Reflected Light

In this section, we will discuss the manifestation of SIA in the linear regime of interaction between optical waves and random metal-dielectric composites: the phase retardation upon reflection of a plane wave and spin-dependent transverse displacement of a reflected beam with finite size. The specific properties of such optical anisotropic composite will be compared to those of the

corresponding isotropic medium characterized using the Maxwell Garnett Effective Medium Theory (MGEM) [131]. It is noted that the SIA of this type of the random composite mainly originates from the local field effect and interaction between metallic inclusions and their own images.

The numerical computation of light propagation through inhomogeneous multiply scattering media was carried out using a numerical Finite Elements Method (Comsol Multiphysics 3.5a). In the numerical experiment, randomly inhomogeneous slabs were illuminated by s- and p-polarized plane waves and the complex reflection and transmission coefficients were derived from the complex field values distributed over the entrance and exit surfaces of the slab. To avoid the influence of evanescent waves on the measured values of the reflected and transmitted waves, the electromagnetic field was evaluated at distances from the slab that were twice larger than the transversal dimensions of the block. The simulation procedure for different spatial distributions of inclusions was repeated in order to determine the values of the average reflection $r_{s,p}$ and transmission $t_{s,p}$ coefficients. In addition, an effective refractive index was estimated using MGEM for the corresponding optically homogeneous slab and the reflection and transmission coefficients were then determined based on the well-defined problem of electromagnetic propagation in thin films [105].

We will begin with a study of phase retardation upon reflection of a plane wave that clearly shows the potential anisotropy of randomly inhomogeneous slabs. It will be later revealed to be an origin of anomalous spin Hall effect of reflected light. We examined the case of an arbitrarily linearly polarized incident plane wave with both s and p components of polarization vector that is reflected by the metal-dielectric composite and by a homogeneous, optically isotropic medium with properties as determined by MGEM. The ellipticity of the reflected wave is defined as the phase difference between the s and p components $(\phi_{r,p} - \phi_{r,s})$,

$$\Delta = \phi_{r,p} - \phi_{r,s} = arg(r_p/r_s) \qquad (25).$$

In our study we investigated the effect of the volume concentration of inclusions dependence on the ellipticity. Approximately 200 realizations with different spatial distribution of inclusions were used to evaluate the average of reflection and transmission coefficients. The calculated phase differences between the s and p components of the optical waves reflected from the composite mediums show clear concentration dependence as seen in Figure 22. The optical anisotropy of the material, intrinsic absorption, and enhanced absorption due to localized surface plasmon resonance [132] are all potential sources of phase difference between the s and p components acquired by the reflection of the metal-dielectric composite. It is worth noting that the interference effect results in sinusoidal-like oscillations in low concentration regime (<4%). However, as can be seen in Figure 22, an increase of absorption as predicted by MGEM diminishes these interferences within the slab leading to only a gradual change of the phase difference at higher concentrations. In the full electromagnetic calculation, the state of polarization of reflected waves from the metal-dielectric composite notably changes in comparison to reflection from the corresponding effective isotropic medium, which is mainly due to the induced anisotropy of this composite. In fact, this trend can be proved by a straightforward calculation in the case of an absorbing anisotropic crystal. However, the degree of optical anisotropy of the random composite is significantly enhanced due to the structural complexity of the inhomogeneous random composite. An enhanced SIA occurs even in low concentration regime (~0-10%) examined here.

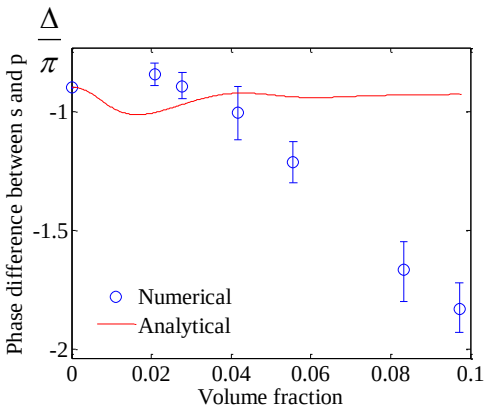

Figure 22 The phase difference between s and p components of the reflected plane wave as a function of volume fraction of 50 nm radius Ag inclusions with refractive index 0.129+3.193i [130] randomly distributed within a host medium with a

thickness of 0.506λ (λ=532 nm) and index of refraction n = 2. Illumination is by a linearly polarized incident plane wave at the angle of incidence 60°. The error bars denote the uncertainty of average values of phase differences with a confidence level 0.95. The red solid line represents the phase difference of the plane wave reflected by a homogeneous medium with effective refractive index estimated by MGEM.

We will now numerically calculate spin dependent lateral displacement (so called "spin Hall effect of light (SHEL)") upon reflection of a finite size beam on the random composite. For an arbitrary linearly polarized beam determined by its horizontal H and vertical V components, the generalized expression for the spatial transverse displacement of the reflected beam in either left (+) or right (-) circularly polarized state is [133]

$$\Delta y_{r\pm} = cos^2\psi_r \Delta y^H_{r\pm} + sin^2\psi_r \Delta y^V_{r\pm} \qquad (26).$$

$$\cos\psi_r = \cos\psi_i Re(r_p)\Big/\sqrt{\cos^2\psi_i Re(r_p)^2 + \sin^2\psi_i Re(r_s)^2}$$

$$\sin\psi_r = \sin\psi_i Re(r_s)\Big/\sqrt{\cos^2\psi_i Re(r_p)^2 + \sin^2\psi_i Re(r_s)^2}$$

$$\Delta y^H_{r\pm} = \mp(\lambda/2\pi)\big[1 + (|r_s|/|r_p|)\cos(\phi_s - \phi_p)\big]\cot\theta_i$$

$$\Delta y^V_{r\pm} = \mp(\lambda/2\pi)\big[1 + (|r_p|/|r_s|)\cos(\phi_p - \phi_s)\big]\cot\theta_i$$

where ψ_r and ψ_i are the reflected and incident polarization angles, respectively, λ is the wavelength in vacuum, and θ_i is the angle of incidence. In Eq. (*26*), $r_{p,s} = |r_{p,s}|\exp(i\phi_{p,s})$ are the reflection coefficients for *p* and *s* polarized plane waves, respectively. It is assumed here that the *y*-axis is normal to the plane of incidence. In the numerical calculations, the metal-dielectric composite effectively behaves as an uniaxial crystal with the optic axis perpendicular to the plane interface. As discussed in[134], the expressions above are modified by substituting r_s and r_p with $r_{s,o}$ and $r_{p,e}$, respectively, with this orientation of the optic axis.

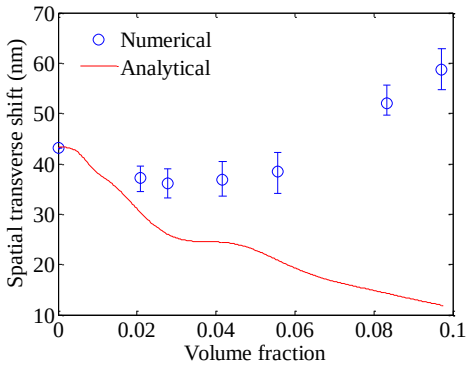

Figure 23 Lateral displacement of the reflected beam, $\Delta \boldsymbol{y}_{\boldsymbol{r}-}$, as a function of the volume concentration of Ag inclusions uniformly embedded in the host medium. The optical properties and dimension of both inclusions and matrix medium are the same as in Figure 22. The metal-dielectric composites with varied concentration of inclusions were illuminated by 45° linearly polarized Gaussian beam at the angle of incidence 60°. The error bars denote the uncertainty of average values of SHEL transverse shift with a confidence level 0.95. The solid line represents the spatial transverse shift of the beam reflected from an effective homogeneous medium with isotropic index estimated by MGEM.

As can be seen in Figure 23, the metal-dielectric composite behaves like an isotropic and homogeneous medium in terms of the induced spatial transverse displacements at low concentration (less than 2%). However, the SHEL shift significantly increases at higher volume concentration of metallic inclusions due to induced optical anisotropy in the random composite. This is due to the fact that the displacement of horizontal polarized component, $\Delta y_{r\pm}^{H}$, experiences the change of sign caused by the large amount of phase difference between the s and p components of reflected waves (see the set of equations (*26*)) as discussed before. In other words, the displacements of both horizontal and vertical polarized components have the same sign and are constructively added to give the unusually large transverse shift.

To sum up, breaking the field symmetry can modify static optical properties of material systems leading to novel linear light-matter interaction. In particular, the surface-induced anisotropy of the metal-dielectric composite caused primarily by the inherent presence of an interface can manifest itself as the anomalous change of the phase difference between the *s* and *p* components and the polarization-dependent transverse shift of reflected waves. With the advantage of its highly flexible fabrication process, the random composite is considered to be a potential material used for controllable spin transport. Such composite with tunable anisotropy also offers matter system in

which unusual physical phenomena including Fano-shaped resonances [135] and the enhanced nanoscale heat flux transfer [136] can be explored.

CHAPTER 5: CONCLUSIONS

Brief Summary of the Past and Present

Symmetry, that is a feature of physical systems, which appears naturally or artificially in many different fields such as architecture, chemistry, or, importantly, in physics. In classical and quantum physics, the symmetry is closely associated with the conservation laws. The conservation laws under the symmetry considerations serve as a general framework to unify the interpretation of the interaction occurring in complex multi-body systems. This approach enables understanding and engineering the intricate interactions which, in turn, lead to different means for controlling spatio-temporal dynamics or for modifying locally the properties of material systems.

Since the advent of laser, light has been widely used to manipulate both colloidal and biological systems in a remote, non-invasive, and precise manner at microscopic scale. The mechanical action of light is a direct consequence of momentum transfer from light to matter. The momentum exchange upon light-matter interaction ensures the conservation of momentum.

The unusual behavior of optical forces acting on objects can be simply understood from the conservation of linear momentum. According to this fundamental law, the total linear momentum of an entire system, comprising both the electromagnetic field and objects, must be conserved. The symmetry breaking of the angular distribution of scattered waves (so called “phase-function”) can unbalance the field momentum that can be transferred to the objects. This can have intriguing mechanical consequences, for instance the transversal forces discussed in Chapter 2. It is worth noting that the field symmetry can be broken both by creating complex structures and by modifying the environment.

In Chapter 2, the breaking of the field symmetry was implemented to purposely demonstrate the action of transversal forces on objects that are isotropic in shape and optical properties. In one situation, the scattering of a micron sized dielectric sphere illuminated by a complex field (two beam configuration) produces the necessary asymmetric phase function. According to the momentum

conservation law, a nonconservative force appears on the spherical particle acting along the direction perpendicular to a plane formed by the propagating vectors of two incident beams. This out-of-plane motion of the particles, that doesn't come from the action of optical gradient force and radiation pressure, demonstrates the unusual behavior of optical force.

There is another way to interpret the existence of this unusual force field component in this optical scattering situation. Upon wave interaction with a particle, the deflection of the resulting scattered pattern arises. To satisfy the *actio et reactio* principle, the shift of the centroid of the intensity distribution results in the mechanical force acting on the center of the mass of the sphere. This consequence can also be regarded as evidence for dynamic effects in the original Aharonov-Bohm setting in which nondissipative mechanical force acts back on the solenoid upon deflection of electron interference pattern. There, the interaction of electron wavefunction with the magnetic vector potential associated with the solenoid's magnetic field was of interest. This analogy should assist in understanding a broad range of phenomena where experiments are almost inaccessible or difficult to conceive.

Later in Chapter 2, it was demonstrated another situation where the symmetry of the electromagnetic field can be broken during the light scattering of a dielectric sphere positioned at the interface between two dielectric media. As a result, the asymmetry of the scattering phase function unbalances the transversal linear momentum. The momentum transfer governed by the conservation of linear momentum gives rise to a lateral force acting on the sphere. This nonconservative optical force can be used to manipulate objects on the surface of liquids without structuring light beams. It is worth emphasizing that the unusual force component arises from the modification of complex fields at dielectric interfaces.

After investigating the interfacial transversal force, we examined the role of the surface on the behavior of the longitudinal component of optical force in Chapter 3. We demonstrated a negative force pulling on floating objects against the flow of light and along the liquid surface. The optical

pulling force arises due to the appropriate amplification of the photon linear momentum when light is scattered from one dielectric medium into another with higher refractive index. This is an opposite to the radiation pressure that usually pushes objects along the direction of the incident wave propagation. It was also shown that the negative force can be generated without resorting to non-paraxial illumination, interference of multiple beams, gain or other exotic materials. Instead, our approach is based on the universal characteristics of optical forces acting on objects moving at the interface between different dielectric media. These results represent a complete set of nonconservative forces that permit arbitrary long-range manipulation of colloidal particles on the liquid surface with unstructured light.

Due to a small magnitude of momentum carried by light and imparted to objects, light usually exerts only tiny forces on microscopic objects. Hence, the experimental detection can become a challenging task considering being immersed in various sources of noises. To circuimvent these limitations, we studied the possibility to amplify the optomechanical effects by harnessing the long-range hydrodynamic interaction between large numbers of manipulated particles. Remarkably, the particle motion mediated by fluid can be significantly enhanced even at low irradiance. From this viewpoint, the concept can be employed to achieve efficient optically controlled transport without resorting to optical absorption and sophisticated photonic structures. The technique can easily be integrated in microfluidic lab-on-chip platforms. Besides, the appropriate treatment of the hydrodynamic interaction can be applied to obtain the correct magnitude of measured optical forces acting on isolated particles based on observed velocities of particles and particle distribution.

This dissertation focuses mostly on the motions of particles as a mechanical consequence of light-matter interaction. However, there are also situations where the force is exerted on the field itself leading to detectable shifts of the centroids of optical beams during light reflection and refraction. Chapter 4 is devoted to spin Hall effect of light that is one type of beam shifts based on the spin-orbit transformation governed by conservation of angular momentum. Due to difficulty to detect

subwavelength beam shifts, it is desired to find novel material that can enhance the Hall-type effects for applications in information processing and communication. We showed that the structural anisotropy of random nanocomposite can manifest itself as the anomalously enhanced SHEL. Different mechanisms nearby surface layer contribute to the induced anisotropy as confirmed by full electrodynamic calculation.

LIST OF PUBLICATIONS

1. S. Sukhov, **V. Kajorndejnukul**, R. R. Naraghi, and A. Dogariu, *Dynamic consequences of optical spin-orbit interaction*, Nature Photonics **9**, doi:10.1038/nphoton.2015.200, (*in press*).

2. **V. Kajorndejnukul**, S. Sukhov, and A. Dogariu, *Efficient mass transport by optical advection*, Sci. Rep. **5**, 14861 (2015).

3. S. Sukhov, **V. Kajorndejnukul**, J. Broky, and A. Dogariu, *Forces in Aharonov–Bohm optical setting*, Optica **1**, 383-387 (2014).

4. **V. Kajorndejnukul**, W. Ding, S. Sukhov, C. W. Qiu, and A. Dogariu, *Linear momentum increase and negative optical forces at dielectric interface*, Nature Photonics **7,** 787–790 (2013).

5. S. Sukhov, D. Haefner, **V. Kajorndejnukul**, G. Agarwal, and A. Dogariu, *Surface-induced optical anisotropy of inhomogeneous media*, Photonics and Nanostructures **11**, 65-72 (2013).

6. **V. Kajorndejnukul**, S. Sukhov, D. Haefner, A. Dogariu, and G. Agarwal, *Surface induced anisotropy of metal–dielectric composites and the anomalous spin Hall effect*, Opt. Lett. **37**, 3036-3038 (2012).

LIST OF PRESENTATIONS

1. **V. Kajorndejnukul**, S. Sukhov, and A. Dogariu, *Optical Advection*, in Frontiers in Optics 2015, OSA Technical Digest (online), paper FTu5F.5 (2015).

2. S. Sukhov, **V. Kajorndejnukul**, R. Rezvani Naraghi, and A. Dogariu, Mechanical Action of Optical Spin-Orbit Interaction, in Frontiers in Optics 2015, OSA Technical Digest (online), paper FTu5F.6 (2015).

3. S. Sukhov, **V. Kajorndejnukul**, J. Broky, and A. Dogariu, *Experimental Detection of Forces in an Optical Analog of Aharonov-Bohm Effect*, in CLEO 2015, OSA Technical Digest (online), paper FM2D.8 (2015).

4. **V. Kajorndejnukul**, S. Sukhov, W. Ding, C. Qiu, and A. Dogariu, *Experimental Demonstration of Negative Optical Forces at Dielectric Interfaces*, in CLEO 2013, OSA Technical Digest (online), paper QM3E.3 (2013).

5. **V. Kajorndejnukul**, S. Sukhov, and A. Dogariu, *Manifestation of Surface Induced Anisotropy: Anomalous spin Hall effect*, in Frontiers in Optics 2012, OSA Technical Digest (online), paper FW5B.3 (2012).

LIST OF REFERENCES

[1] E. Greenfield, J. Nemirovsky, R. El-Ganainy, D.N. Christodoulides, M. Segev, Shockwave based nonlinear optical manipulation in densely scattering opaque suspensions, Opt. Express, 21 (2013) 23785-23802.

[2] J. Gordon, Radiation Forces and Momenta in Dielectric Media, Physical Review A, 8 (1973) 14-21.

[3] R. Loudon, Radiation pressure and momentum in dielectrics, Fortschritte der Physik, 52 (2004) 1134-1140.

[4] R. Pfeifer, T. Nieminen, N. Heckenberg, H. Rubinsztein-Dunlop, Colloquium: Momentum of an electromagnetic wave in dielectric media, Reviews of Modern Physics, 79 (2007) 1197-1216.

[5] E. Hinds, S. Barnett, Momentum Exchange between Light and a Single Atom: Abraham or Minkowski?, Physical Review Letters, 102 (2009).

[6] S.M. Barnett, Resolution of the Abraham-Minkowski Dilemma, Physical Review Letters, 104 (2010).

[7] S.M. Barnett, R. Loudon, The enigma of optical momentum in a medium, Philosophical Transactions of the Royal Society A: Mathematical, Physical and Engineering Sciences, 368 (2010) 927-939.

[8] M. Mansuripur, Resolution of the Abraham–Minkowski controversy, Optics Communications, 283 (2010) 1997-2005.

[9] C. Baxter, R. Loudon, Radiation pressure and the photon momentum in dielectrics, Journal of Modern Optics, 57 (2010) 830-842.

[10] P.W. Milonni, R.W. Boyd, Momentum of Light in a Dielectric Medium, Advances in Optics and Photonics, 2 (2010) 519.

[11] R.N.C. Pfeifer, T.A. Nieminen, N.R. Heckenberg, H. Rubinsztein-Dunlop, Optical tweezers and paradoxes in electromagnetism, Journal of Optics, 13 (2011) 044017.

[12] B.A. Kemp, Resolution of the Abraham-Minkowski debate: Implications for the electromagnetic wave theory of light in matter, Journal of Applied Physics, 109 (2011) 111101.

[13] A. Ashkin, J. Dziedzic, J. Bjorkholm, S. Chu, Observation of a single-beam gradient force optical trap for dielectric particles, Optics letters, 11 (1986) 288-290.

[14] A. Ashkin, Forces of a single-beam gradient laser trap on a dielectric sphere in the ray optics regime, Biophysical journal, 61 (1992) 569-582.

[15] K. Dholakia, T. Čižmár, Shaping the future of manipulation, Nature Photonics, 5 (2011) 335-342.

[16] A. Ashkin, J.P. Gordon, Stability of radiation-pressure particle traps: an optical Earnshaw theorem, Optics letters, 8 (1983) 511-513.

[17] D.G. Grier, A revolution in optical manipulation, Nature, 424 (2003) 810-816.

[18] C.F. Bohren, D.R. Huffman, Absorption and scattering of light by small particles, Wiley. com, 2008.

[19] J. Chen, J. Ng, Z. Lin, C.T. Chan, Optical pulling force, Nature Photonics, 5 (2011) 531-534.

[20] R. Gómez-Medina, Electric and magnetic dipolar response of germanium nanospheres: interference effects, scattering anisotropy, and optical forces, Journal of Nanophotonics, 5 (2011) 053512.

[21] A. García-Etxarri, R. Gómez-Medina, L. Froufe-Pérez, C. López, L. Chantada, F. Scheffold, J. Aizpurua, M. Nieto-Vesperinas, J. Sáenz, Strong magnetic response of submicron Silicon particles in the infrared, Optics Express, 19 (2011) 4815-4826.

[22] O. Brzobohatý, V. Karásek, M. Šiler, L. Chvátal, T. Čižmár, P. Zemánek, Experimental demonstration of optical transport, sorting and self-arrangement using a/tractor beam/', Nature Photonics, (2013).

[23] S. Sukhov, A. Dogariu, Negative Nonconservative Forces: Optical "Tractor Beams" for Arbitrary Objects, Physical Review Letters, 107 (2011).

[24] A.P. Mosk, A. Lagendijk, G. Lerosey, M. Fink, Controlling waves in space and time for imaging and focusing in complex media, Nature photonics, 6 (2012) 283-292.

[25] C.E. Démoré, P.M. Dahl, Z. Yang, P. Glynne-Jones, A. Melzer, S. Cochran, M.P. MacDonald, G.C. Spalding, Acoustic tractor beam, Physical review letters, 112 (2014) 174302.

[26] A. Dogariu, S. Sukhov, J. Sáenz, Optically induced 'negative forces', Nature Photonics, 7 (2012) 24-27.

[27] R.A. Beth, Mechanical detection and measurement of the angular momentum of light, Physical Review, 50 (1936) 115.

[28] L. Allen, M. Beijersbergen, R. Spreeuw, J. Woerdman, Orbital angular momentum of light and the transformation of Laguerre-Gaussian laser modes, Physical Review A, 45 (1992) 8185-8189.

[29] A. O'neil, I. MacVicar, L. Allen, M. Padgett, Intrinsic and extrinsic nature of the orbital angular momentum of a light beam, Physical review letters, 88 (2002) 053601.

[30] M. Padgett, R. Bowman, Tweezers with a twist, Nature Photonics, 5 (2011) 343-348.

[31] M. Friese, T. Nieminen, N. Heckenberg, H. Rubinsztein-Dunlop, Optical alignment and spinning of laser-trapped microscopic particles, Nature, 394 (1998) 348-350.

[32] E. Higurashi, H. Ukita, H. Tanaka, O. Ohguchi, Optically induced rotation of anisotropic micro-objects fabricated by surface micromachining, Applied physics letters, 64 (1994) 2209-2210.

[33] P. Galajda, P. Ormos, Complex micromachines produced and driven by light, Applied Physics Letters, 78 (2001) 249-251.

[34] N. Simpson, K. Dholakia, L. Allen, M. Padgett, Mechanical equivalence of spin and orbital angular momentum of light: an optical spanner, Optics Letters, 22 (1997) 52-54.

[35] J. Leach, H. Mushfique, R. di Leonardo, M. Padgett, J. Cooper, An optically driven pump for microfluidics, Lab on a chip, 6 (2006) 735-739.

[36] K.Y. Bliokh, A. Aiello, Goos–Hänchen and Imbert–Fedorov beam shifts: an overview, Journal of Optics, 15 (2013) 014001.

[37] D. Haefner, S. Sukhov, A. Dogariu, Spin hall effect of light in spherical geometry, Physical review letters, 102 (2009) 123903.

[38] O. Hosten, P. Kwiat, Observation of the spin Hall effect of light via weak measurements, Science, 319 (2008) 787-790.

[39] S. Sukhov, V. Kajorndejnukul, J. Broky, A. Dogariu, Forces in Aharonov–Bohm optical setting, Optica, 1 (2014) 383-387.

[40] M. Berry, R. Chambers, M. Large, C. Upstill, J. Walmsley, Wavefront dislocations in the Aharonov-Bohm effect and its water wave analogue, European Journal of Physics, 1 (1980) 154.

[41] R.J. Cook, H. Fearn, P.W. Milonni, Fizeau's experiment and the Aharonov-Bohm effect, American Journal of Physics, 63 (1995) 705-709.

[42] E. Sonin, The Aharonov–Bohm effect in neutral liquids, Journal of Physics A: Mathematical and Theoretical, 43 (2010) 354003.

[43] C. Coste, F. Lund, M. Umeki, Scattering of dislocated wave fronts by vertical vorticity and the Aharonov-Bohm effect. I. Shallow water, Physical Review E, 60 (1999) 4908.

[44] M. Vieira, A.M.d.M. Carvalho, C. Furtado, Aharonov-Bohm effect for light in a moving medium, Physical Review A, 90 (2014) 012105.

[45] S. Iordansky, On the mutual friction between the normal and superfluid components in a rotating Bose gas, Annals of Physics, 29 (1964) 335-349.

[46] M. Stone, Iordanskii force and the gravitational Aharonov-Bohm effect for a moving vortex, Physical Review B, 61 (2000) 11780.

[47] U. Leonhardt, P. Öhberg, Optical analog of the Iordanskii force in a Bose-Einstein condensate, Physical Review A, 67 (2003) 053616.

[48] D. Neshev, A. Nepomnyashchy, Y.S. Kivshar, Nonlinear Aharonov-Bohm scattering by optical vortices, Physical review letters, 87 (2001) 043901.

[49] K. Fang, Z. Yu, S. Fan, Photonic Aharonov-Bohm effect based on dynamic modulation, Physical review letters, 108 (2012) 153901.

[50] E. Li, B.J. Eggleton, K. Fang, S. Fan, Photonic Aharonov–Bohm effect in photon–phonon interactions, Nature communications, 5 (2014).

[51] C. Dartora, K. Nobrega, G. Cabrera, Optical analogue of the Aharonov–Bohm effect using anisotropic media, Physics Letters A, 375 (2011) 2254-2257.

[52] C. Tan, Aharonov–Bohm effect in optical activity, Journal of Physics A: Mathematical and Theoretical, 43 (2010) 354007.

[53] S. Longhi, Aharonov–Bohm photonic cages in waveguide and coupled resonator lattices by synthetic magnetic fields, Optics letters, 39 (2014) 5892-5895.

[54] Y. Gorodetski, S. Nechayev, V. Kleiner, E. Hasman, Plasmonic Aharonov-Bohm effect: Optical spin as the magnetic flux parameter, Physical Review B, 82 (2010) 125433.

[55] S. Olariu, I.I. Popescu, The quantum effects of electromagnetic fluxes, Reviews of Modern Physics, 57 (1985) 339-436.

[56] R. Feynman, R. Leighton, M. Sands, The Feynman: Lectures on Physics, Mainly Electromagnetism and Matter. Vol. 2. 1963, in, New York: Addison-Wesley Publishing Co.

[57] M.D. Semon, J.R. Taylor, The Aharonov-Bohm effect: still a thought-provoking experiment, Foundations of physics, 18 (1988) 731-740.

[58] A. Shelankov, Magnetic force exerted by the Aharonov-Bohm line, EPL (Europhysics Letters), 43 (1998) 623.

[59] M. Berry, Aharonov-Bohm beam deflection: Shelankov's formula, exact solution, asymptotics and an optical analogue, Journal of Physics A: Mathematical and General, 32 (1999) 5627.

[60] A. Dogariu, C. Schwartz, Conservation of angular momentum of light in single scattering, Optics express, 14 (2006) 8425-8433.

[61] A. Béché, R. Van Boxem, G. Van Tendeloo, J. Verbeeck, Magnetic monopole field exposed by electrons, Nature Physics, 10 (2014) 26-29.

[62] F. Borghese, P. Denti, R. Saija, Scattering from model nonspherical particles: theory and applications to environmental physics, Springer Science & Business Media, 2007.

[63] U. Leonhardt, P. Piwnicki, Relativistic Effects of Light in Moving Media with Extremely Low Group Velocity, Physical Review Letters, 84 (2000) 822-825.

[64] M. Berry, P. Shukla, Classical dynamics with curl forces, and motion driven by time-dependent flux, Journal of Physics A: Mathematical and Theoretical, 45 (2012) 305201.

[65] V. Fedoseyev, Transverse forces related to the transverse shifts of reflected and transmitted light beams, Journal of Optics, 15 (2013) 014017.

[66] V. Kajorndejnukul, W. Ding, S. Sukhov, C.-W. Qiu, A. Dogariu, Linear momentum increase and negative optical forces at dielectric interface, Nature Photonics, 7 (2013) 787-790.

[67] P. Chaumet, M. Nieto-Vesperinas, Time-averaged total force on a dipolar sphere in an electromagnetic field, Optics letters, 25 (2000) 1065-1067.

[68] L. Novotny, B. Hecht, Principles of nano-optics, Cambridge university press, 2012.

[69] S. Wang, C. Chan, Lateral optical force on chiral particles near a surface, Nature communications, 5 (2014).

[70] D. Haefner, S. Sukhov, A. Dogariu, Conservative and nonconservative torques in optical binding, Physical review letters, 103 (2009) 173602.

[71] A.Y. Bekshaev, O. Angelsky, S.G. Hanson, C.Y. Zenkova, Scattering of inhomogeneous circularly polarized optical field and mechanical manifestation of the internal energy flows, Physical Review A, 86 (2012) 023847.

[72] A. Salandrino, S. Fardad, D.N. Christodoulides, Generalized Mie theory of optical forces, JOSA B, 29 (2012) 855-866.

[73] A.Y. Bekshaev, K.Y. Bliokh, F. Nori, Transverse spin and momentum in two-wave interference, Physical Review X, 5 (2015) 011039.

[74] S. Omenyi, A. Neumann, C. Van Oss, Attraction and repulsion of solid particles by solidification fronts I. Thermodynamic effects, Journal of Applied Physics, 52 (1981) 789-795.

[75] R. Wunenburger, B. Issenmann, E. Brasselet, C. Loussert, V. Hourtane, J.-P. Delville, Fluid flows driven by light scattering, Journal of Fluid Mechanics, 666 (2011) 273-307.

[76] V. Kajorndejnukul, S. Sukhov, A. Dogariu, Efficient mass transport by optical advection, Scientific reports, 5 (2015).

[77] J. Rotne, S. Prager, Variational treatment of hydrodynamic interaction in polymers, The Journal of Chemical Physics, 50 (1969) 4831-4837.

[78] K. Ladavac, D.G. Grier, Colloidal hydrodynamic coupling in concentric optical vortices, EPL (Europhysics Letters), 70 (2005) 548.

[79] J. Happel, H. Brenner, Low Reynolds number hydrodynamics: with special applications to particulate media, Springer Science & Business Media, 2012.

[80] K. Danov, R. Aust, F. Durst, U. Lange, Influence of the surface viscosity on the hydrodynamic resistance and surface diffusivity of a large Brownian particle, Journal of colloid and interface science, 175 (1995) 36-45.

[81] D. Pilat, P. Papadopoulos, D. Schaffel, D. Vollmer, R. Berger, H.-J. Butt, Dynamic measurement of the force required to move a liquid drop on a solid surface, Langmuir, 28 (2012) 16812-16820.

[82] J.C. Crocker, D.G. Grier, Methods of digital video microscopy for colloidal studies, Journal of colloid and interface science, 179 (1996) 298-310.

[83] D.B. Ruffner, D.G. Grier, Optical Conveyors: A Class of Active Tractor Beams, Physical Review Letters, 109 (2012).

[84] A. Ashkin, J. Dziedzic, Radiation Pressure on a Free Liquid Surface, Physical Review Letters, 30 (1973) 139-142.

[85] P.-G. De Gennes, F. Brochard-Wyart, D. Quéré, Capillarity and wetting phenomena: drops, bubbles, pearls, waves, Springer Science & Business Media, 2004.

[86] P. Pieranski, Two-dimensional interfacial colloidal crystals, Physical Review Letters, 45 (1980) 569.

[87] B. Radoev, M. Nedyalkov, V. Dyakovich, Brownian motion at liquid-gas interfaces. 1. Diffusion coefficients of macroparticles at pure interfaces, Langmuir, 8 (1992) 2962-2965.

[88] M. Mansuripur, Radiation pressure and the linear momentum of the electromagnetic field, Opt. Express, 12 (2004) 5375-5401.

[89] K.M. Douglass, S. Sukhov, A. Dogariu, Superdiffusion in optically controlled active media, Nature Photon., 6 (2012) 834-837.

[90] V. Varadan, V. Bringi, V. Varadan, A. Ishimaru, Multiple scattering theory for waves in discrete random media and comparison with experiments, Radio Sci., 18 (1983) 321-327.

[91] A. Ashkin, J.M. Dziedzic, P.W. Smith, Continuous-wave self-focusing and self-trapping of light in artificial Kerr media, Opt. Lett., 7 (1982) 276-278.

[92] J. Happel, H. Brenner, Low Reynolds number hydrodynamics: with special applications to particulate media, Martinus Nijhoff, The Hague, 1983.

[93] A.Y. Savchenko, N. Tabiryan, B.Y. Zel'dovich, Transfer of momentum and torque from a light beam to a liquid, Phys. Rev. E, 56 (1997) 4773.

[94] R. Wunenburger, B. Issenmann, E. Brasselet, C. Loussert, V. Hourtane, J.-P. Delville, Fluid flows driven by light scattering, J. Fluid Mech., 666 (2011) 273-307.

[95] H. Chraibi, R. Wunenburger, D. Lasseux, J. Petit, J.-P. Delville, Eddies and interface deformations induced by optical streaming, J. Fluid Mech., 688 (2011) 195-218.

[96] B.T. Draine, P.J. Flatau, Discrete-dipole approximation for scattering calculations, J. Opt. Soc. Am. A, 11 (1994) 1491-1499.

[97] W. Chen, S. Tan, Z. Huang, T.-K. Ng, W.T. Ford, P. Tong, Measured long-ranged attractive interaction between charged polystyrene latex spheres at a water-air interface, Phys. Rev. E, 74 (2006) 021406.

[98] F. Ortega, H. Ritacco, R.G. Rubio, Interfacial microrheology: particle tracking and related techniques, Curr. Opin. Colloid Interface Sci., 15 (2010) 237-245.

[99] S.N. Omenyi, A.W. Neumann, C.J. van Oss, Attraction and repulsion of solid particles by solidification fronts I. Thermodynamic effects, J. Appl. Phys., 52 (1981) 789-795.

[100] X. Wang, K. Xiao, C. Min, Q. Zou, Y. Hua, X.-C. Yuan, Theoretical and Experimental Study of Surface Plasmon Radiation Force on Micrometer-Sized Spheres, Plasmonics, 8 (2013) 637-643.

[101] S. Kawata, T. Sugiura, Movement of micrometer-sized particles in the evanescent field of a laser beam, Opt. Lett., 17 (1992) 772-774.

[102] S. Kawata, T. Tani, Optically driven Mie particles in an evanescent field along a channeled waveguide, Opt. Lett., 21 (1996) 1768-1770.

[103] K.J. Solis, J.E. Martin, Isothermal Magnetic Advection: Creating functional fluid flows for heat and mass transfer, Appl. Phys. Lett., 97 (2010) 034101.

[104] K.J. Solis, J.E. Martin, Controlling the column spacing in isothermal magnetic advection to enable tunable heat and mass transfer, J. Appl. Phys., 112 (2012) 094912.

[105] M. Born, E. Wolf, Principles of optics: electromagnetic theory of propagation, interference and diffraction of light, CUP Archive, 1999.

[106] F. Goos, H. Hänchen, Ein neuer und fundamentaler Versuch zur Totalreflexion, Annalen der Physik, 436 (1947) 333-346.

[107] F.I. Fedorov, To the theory of total reflection, Dokl. Akad. Nauk SSSR, 105 (1955) 465.

[108] M. Onoda, S. Murakami, N. Nagaosa, Hall Effect of Light, Physical Review Letters, 93 (2004) 083901.

[109] K.Y. Bliokh, Y.P. Bliokh, Conservation of Angular Momentum, Transverse Shift, and Spin Hall Effect in Reflection and Refraction of an Electromagnetic Wave Packet, Physical Review Letters, 96 (2006) 073903.

[110] K.Y. Bliokh, Y.P. Bliokh, Polarization, transverse shifts, and angular momentum conservation laws in partial reflection and refraction of an electromagnetic wave packet, Physical Review E, 75 (2007) 066609.

[111] X. Yin, Z. Ye, J. Rho, Y. Wang, X. Zhang, Photonic spin Hall effect at metasurfaces, Science, 339 (2013) 1405-1407.

[112] S. Sukhov, D. Haefner, V. Kajorndejnukul, G. Agarwal, A. Dogariu, Surface-induced optical anisotropy of inhomogeneous media, Photonics and Nanostructures - Fundamentals and Applications, 11 (2013) 65-72.

[113] J.P. Landry, X. Wang, Y.Y. Fei, X.D. Zhu, Effective-substrate theory for optical reflection from a layered substrate, J. Opt. Soc. Am. B, 25 (2008) 2021-2028.

[114] A. Shvartsburg, V. Kuzmiak, G. Petite, Polarization-dependent tunneling of light in gradient optics, Physical Review E, 76 (2007) 016603.

[115] J. Lafait, T. Yamaguchi, J.M. Frigerio, A. Bichri, K. Driss-Khodja, Effective medium equivalent to a symmetric multilayer at oblique incidence, Applied Optics, 29 (1990) 2460-2465.

[116] O. Gadomskiĭ, S. Sukhov, Microscopic theory of a transition layer on the ideal surface of semiinfinite dielectric media and the near-field effect, Optics and Spectroscopy, 89 (2000) 261-267.

[117] A.D. Scher, E.F. Kuester, Boundary effects in the electromagnetic response of a metamaterial in the case of normal incidence, Progress In Electromagnetics Research B, 14 (2009) 341-381.

[118] I. Romero, F.J. GarcÝa de Abajo, Anisotropy and particle-size effects in nanostructured plasmonic metamaterials, Optics express, 17 (2009) 22012-22022.

[119] C.R. Simovski, Material parameters of metamaterials (a Review), Optics and Spectroscopy, 107 (2009) 726-753.

[120] C.R. Simovski, On electromagnetic characterization and homogenization of nanostructured metamaterials, Journal of Optics, 13 (2011) 013001.

[121] S. Tretyakov, Analytical modeling in applied electromagnetics, Artech House, 2003.

[122] M. Born, Dynamical theory of crystal lattices, (1966).

[123] P. Drude, The theory of optics, Courier Corporation, 1925.

[124] A. Sommerfeld, Optics, Academic, New York, (1954) 180.

[125] S. Sukhov, D. Haefner, A. Dogariu, Coupled dipole method for modeling optical properties of large-scale random media, Physical Review E, 77 (2008) 066709.

[126] N. Stefanou, V. Yannopapas, A. Modinos, Heterostructures of photonic crystals: frequency bands and transmission coefficients, Computer physics communications, 113 (1998) 49-77.

[127] D.R. Smith, S. Schultz, P. Markoš, C.M. Soukoulis, Determination of effective permittivity and permeability of metamaterials from reflection and transmission coefficients, Physical Review B, 65 (2002) 195104.

[128] C. Menzel, C. Rockstuhl, T. Paul, F. Lederer, T. Pertsch, Retrieving effective parameters for metamaterials at oblique incidence, Physical Review B, 77 (2008) 195328.

[129] D.J. Bergman, Bounds for the complex dielectric constant of a two-component composite material, Physical Review B, 23 (1981) 3058-3065.

[130] E.D. Palik, Handbook of optical constants of solids, Academic press, 1998.

[131] J. MAXWELL GARNETT, Effective medium models for the optical properties of inhomogeneous media, Philos. Trans. R. Soc. London, 203 (1904).

[132] E. Hutter, J.H. Fendler, Exploitation of localized surface plasmon resonance, Advanced Materials, 16 (2004) 1685-1706.

[133] H. Luo, X. Ling, X. Zhou, W. Shu, S. Wen, D. Fan, Enhancing or suppressing the spin Hall effect of light in layered nanostructures, Physical Review A, 84 (2011) 033801.

[134] Y. Qin, Y. Li, X. Feng, Z. Liu, H. He, Y.-F. Xiao, Q. Gong, Spin Hall effect of reflected light at the air-uniaxial crystal interface, Optics express, 18 (2010) 16832-16839.

[135] C.-W. Qiu, A. Novitsky, L. Gao, J.-W. Dong, B. Luk'yanchuk, Anisotropy-induced Fano resonance, arXiv preprint arXiv:1202.5613, (2012).

[136] S.A. Biehs, P. Ben-Abdallah, F.S.S. Rosa, K. Joulain, J.J. Greffet, Nanoscale heat flux between nanoporous materials, Optics Express, 19 (2011) A1088-A1103.